
Article:
Vahl, A, Lupan, O, Santos-Carballal, D orcid.org/0000-0002-3199-9588 et al. (12 more authors) (2020) Surface functionalization of ZnO:Ag columnar thin films with AgAu and AgPt bimetallic alloy nanoparticles as an efficient pathway for highly sensitive gas discrimination and early hazard detection in batteries. Journal of Materials Chemistry A. ISSN 2050-7488

https://doi.org/10.1039/D0TA03224G

Journal of Materials Chemistry A

PAPER

Surface functionalization of ZnO:Ag columnar thin films with AgAu and AgPt bimetallic alloy nanoparticles as an efficient pathway for highly sensitive gas discrimination and early hazard detection in batteries

Received 00th January 20xx,
Accepted 00th January 20xx

DOI: 10.1039/x0xx00000x

www.rsc.org/

Alexander Vahl,[a] Oleg Lupan,[b,c,†] David Santos-Carballal,[*,d,e,†] Vasile Postica,[c] Sandra Hansen,[b] Heather Cavers,[b] Niklas Wolff,[f] Maik-Ivo Terasa,[b] Mathias Hoppe,[b] Abdelaziz Cadi-Essadek,[e] Torben Dankwort,[f] Lorenz Kienle,[f] Nora H. de Leeuw,[*,d,g,†] Rainer Adelung,[b,†] Franz Faupel [a,†]

For a fast and reliable monitoring of hazardous environments, the discrimination and detection of volatile organic compounds (VOCs) in the low ppm range is critical~~highly demanded~~ly important, which ~~and~~ requires the development of new chemical sensors. We report herein~~,~~ a novel approach to tailor the selectivity of nanocomposite thin film sensors by investigating systematically the effect of surface decoration of Ag-doped ZnO (ZnO:Ag) columnar thin films. We have used AgPt and AgAu noble bimetallic alloy nanoparticles (NPs) to decorate the surfaces of ZnO:Ag and we have measured their resulting gas sensing properties towards VOC vapors and hydrogen gas. The gas response of the nanocomposite containing AgAu NPs to 100 ppm of ethanol, acetone, *n*-butanol, 2-propanol and methanol vapors was increased on average by a factor of 4 compared to the pristine ZnO:Ag columnar films. However, decoration with AgPt NPs led to a considerable reduction of the gas response to all VOC vapors and an increase of the response to H_2 by roughly one order of magnitude, indicating a possibile route to tailor the selectivity by surface decoration. As such~~For this reason~~, the reported NP-decorated ZnO:Ag thin film sensors should be~~are~~ suitable for the detection of H_2 in Li-ion batteries, which is an early indication of the thermal runaway that leads to complete battery failure and possible explosion. To understand the impact of NP surface decoration on the gas sensing properties of ZnO:Ag thin films, we have employed density functional theory calculations with on-site Coulomb corrections and long-range dispersion interactions (DFT+*U*–D3-(BJ)) to ~~and~~ investigate~~d~~ the adsorption of various VOC molecules and hydrogen onto the Ag-doped and NP-decorated $(10\bar{1}0)$ surface of zinc oxide ZnO. The calculated surface free energies indicate that Ag_5Au_5/ZnO$(10\bar{1}0)$:Ag is the most favourable system for the detection of VOCs, which based on its work function is also the most reactive towards these species~~m based on its work function~~. Our calculated adsorption energies show that Ag_9Pt/ZnO$(10\bar{1}0)$:Ag has the largest preference for H_2 and the lowest preference for the organic asdorbates, which is in line with the high selectivity of AgPt/ZnO:Ag sensors towards the hydrogen ~~former~~ molecule observed in our experiments.

Introduction

Nanocomposites that consist of noble metal nanoparticles (NPs) and micro- and nano-structures of semiconducting oxides, such as ZnO, SnO_2 and CuO, have attracted significant attention~~research interest~~ for their potentially highly sensitive detection of gases and VOC vapors,[1-3] owing~~due~~ to their excellent electronic, catalytic and optical properties.[4] S~~T~~he surface decoration by NPs has shown to affect many sensor characteristics, including: (i) the sensitivity, enabling the detection of even trace amounts of gases; (ii) the selectivity towards certain gaseous species; (iii) the response and recovery times, which have been substantially reduced; and (iv) the acceptable~~usable~~ operating temperatures, which have been shifted to values close to ambient conditions.[1, 5-7] Recently, highly sensitive and selective hydrogen gas nano-sensors have been ~~were~~ described

[a]Institute for Materials Science – Chair for Multicomponent Materials, Faculty of Engineering, Christian-Albrechts-University of Kiel, Kaiserstraße 2, D-24143 Kiel, Germany
[b]Institute for Materials Science – Functional Nanomaterials, Faculty of Engineering, Christian-Albrechts-University of Kiel, Kaiserstraße 2, D-24143 Kiel, Germany
[c]Center for Nanotechnology and Nanosensors, Department of Microelectronics and Biomedical Engineering, Technical University of Moldova, 168 Stefan cel Mare Av., MD-2004 Chisinau, Republic of Moldova
[d]School of Chemistry, University of Leeds, Leeds LS2 9JT, United Kingdom.
[e]School of Chemistry, Cardiff University, Main Building, Park Place, Cardiff CF10 3AT, United Kingdom.
[f]Institute for Materials Science – Synthesis and Real Structure, Christian-Albrechts-University of Kiel, Kaiserstraße 2, D-24143 Kiel, Germany
[g]Department of Earth Sciences, Utrecht University, Princetonplein 8A, 3584 CB Utrecht, The Netherlands.
† Prof. Dr. Rainer Adelung, ra@tf.uni-kiel.de.; Prof. Dr. Franz Faupel, ff@tf.uni-kiel.de; Prof. Oleg Lupan, ollu@tf.uni-kiel.de, oleg.lupan@mib.utm.md; Dr. David Santos-Carballal, D.Santos-Carballal@leeds.ac.uk; Prof. Nora H. de Leeuw, N.H.deLeeuw@leeds.ac.uk, n.h.deleeuw@uu.nl;
Electronic Supplementary Information (ESI) available: [details of any supplementary information available should be included here]. See DOI: 10.1039/x0xx00000x

that are based on individual ZnO nanowires decorated by Pd NPs.[1, 5] Guo *et al.* reported a remarkable enhancement of the gas sensing properties of ZnO nanorods by surface decoration with Au NPs, leading to fast response and recovery times, good selectivity and stable repeatability.[6, 8] Majhi *et al.* have successfully prepared Au@ZnO core-shell NPs by a facile low-temperature solution route for highly selective H_2 gas detection, which was attributed to the chemical as well as catalytic effect of Au NPs.[7]

However, recent results have demonstrated that bimetallic NPs have unique physico-chemical properties, superior to their monometallic counterparts, owing to the combination of their unique and the induced synergistic effects.[4, 9-11] Yong *et al.* have used density functional theory calculations to investigate the adsorption of CO, HCN and NO on Ag_7Au_6 clusters for potential application as gas sensors and they found that adsorbates chemisorb on the surface of clusters with exothermic adsorption energies and finite charge transfer.[10] Choi *et al.* decorated SnO_2 nanowire networks with bimetallic PtPd NPs, which led to fast response and recovery times during the detection of NO_2.[12] Fan *et al.* prepared ZnO loaded with PtAu bimetallic NPs, which showed high sensitivity to hydrogen down to the ppm-level, even at room temperature,[13] whereas Hassan *et al.* decorated ZnO nanorods with PtPd bimetallic core-shell NPs for accelerated hydrogen gas detection.[14]

Thus, it is crucially important to develop a technological approach which can control alloyed NP properties[9] and to investigate the gas sensing performance of decorated nanocomposites comprising micro- and nanostructured semiconducting oxides and bimetallic NPs. The Ag-based alloys, such as AgPt and AgAu, are of particular interest due to the synergistic effect between the noble metal components, which makes them appealing for surface-enhanced Raman spectroscopy (SERS) as well as for applications in photocatalysis and sensing.[4,15,16] Ag-based NPs have several advantages compared to other noble metals, e.g. harboring more active sites on their surface, which facilitates a more efficient electron transfer during the gas sensing applications.[15] Ag-containing NPs are also more cost-effective in their preparation than their monometallic counterparts.[15] Bimetallic AgAu NPs display a distinctive optical plasmon absorbance in the visible range[17]. Their monometallic components have very similar lattice constants (4.09 Å for Ag and 4.08 Å for Au), allowing the preparation of different core–shell structures as well as alloys down to an average diameter of 4 – 5 nm,[17] which are in high demand for device applications.

Despite the significant~~great~~ potential, the effect~~influence~~ of AgAu and AgPt NPs decorating the surface ~~surface decoration~~ of semiconducting oxide micro- and nano-structures, especially columnar films, has not received much~~enough~~ attention. Therefore, in the present study, nanocomposites were prepared by the decoration of Ag-doped ZnO columnar thin films (ZnO:Ag) with AgAu and AgPt NPs. Their gas sensing properties with regard to different VOCs and hydrogen gas were studied in detail. AgAu NP-decorated sensors showed a significant increase in sensitivity towards VOCs compared to the pristine ZnO:Ag nanostructured films, whereas ~~.t~~The AgPt-decorated sensors showed a change in the selectivity from VOCs to H_2 gas.

Furthermore, we can place the concept of noble metal alloy NP nanocomposite sensors in the context of early hazard detection in Li ion batteries (LIB). In this particular application scenario, the fast and reliable detection of H_2 gas is especially important for the operation of battery modules that contain a large number of cells in parallel. The electrolytes are composed of a lithium salt and aprotic organic solvents, typically organic carbonates or ether solvents, which can produce H_2 gas as a decomposition product.[18-20] In this case, single battery cells inside a larger module experience degradation and a rise in internal temperature to a critical point, which is likely to have a catastrophic effect on the performance of adjacent cells. In addition, in events like the sudden penetration or puncturing of the battery, the commonly used organic carbonate electrolytes decompose and produce large quantities of H_2 gas, alongside a temperature increase of up to 200-250 °C. Thus, there is urgent demand for an immediate detection system with the potential for direct integration into the individual cells to avoid complete battery failure. In this study, the high sensitivity and fast response times of AgPt NP nanocomposite sensors is related to a potential application in this scenario.

Finally, the corresponding gas sensing mechanisms are proposed and supported by an extensive theoretical investigation. To uncover the origin of the unique gas sensing properties of the alloy NP-decorated ZnO:Ag thin films, first principles simulations were applied to study the sensing properties towards VOCs of the Ag-doped ZnO ($\mathbf{10\bar{1}0}$) surface decorated with Ag_5Au_5 and Ag_9Pt clusters, where the metal ratios were chosen to reflect similar ratios as the experimentally obtained AgPt and AgAu NPs. The adsorption energies, electronic and structural implications of different scenarios have been investigated for the substitutional doping and adsorption of the alloy metal clusters onto the surface. Furthermore, the binding of ethanol, acetone, *n*-butanol, 2-propanol, methanol and molecular hydrogen on the ZnO:Ag as well as the Ag_9Pt/ZnO:Ag and Ag_5Au_5/ZnO:Ag modified surfaces are discussed to account for changes in selectivity and sensitivity. Whereas the sensitivity towards the VOC molecules was increased by the surfaces decorated with Ag_5Au_5 NPs, the Pt-based alloy NPs changed the nanocomposite's selectivity to H_2 gas, in correspondence with the experiment.

Experimental

Sample synthesis

Ag-doped ZnO nanostructured columnar thin films (ZnO:Ag) with a nominal thickness of 1.5 µm were deposited on glass substrates by a simple and inexpensive synthesis method from chemical solutions (SCS). Details of the SCS method used to create the doped ZnO columnar films were presented in previous works.[21-24] The Ag doping content in the prepared samples was adjusted to 0.95 $\%_{wt}$, which was confirmed in an earlier investigation by energy-dispersive X-ray (EDX) spectroscopy and X-ray photoelectron spectroscopy (XPS).[25] All samples were thermally annealed at 650 °C for 2 h in air after deposition.

The alloy NPs were deposited onto the ZnO:Ag columnar thin films and Si wafer pieces (for reference measurements, Si-Mat, 10x10 mm²) using a custom-built high vacuum deposition system

with an in-house Haberland type Gas Aggregation Source (GAS).[26-28] For the generation of the AgAu and AgPt bimetallic alloy NPs, customized silver targets (Kurt J. Lesker, 99.99 %, 50.8 mm diameter) were used, with a drilled trench and a fitted Au wire (Alfa Aesar, 1.0 mm diameter, 99.95%) or Pt wire (Alfa Aesar, 1.0mm diameter, 99.95%), respectively. The deposition of alloy NPs by applying the target geometry methodology has been characterized in detail in an earlier work.[29] A photograph depicting both targets in the geometry used is given in **Figure 1a**), while the whole PVD setup is sketched in **Figure 1b**). The respective target is mounted onto a DC planar magnetron source (Thin Film Consulting, ION'X-2UHV). Prior to deposition, the HV deposition system was evacuated to at least 10^{-4} Pa using a turbo molecular pump (Pfeiffer Vacuum, TMU 262) and a dry scroll pump (Agilent Technologies, SH-110). For sputtering, an Ar flow of 48 sccm, (purity 99.999%) was supplied at the gas inlet near ~~to~~ the target (gas regulating valve: Pfeiffer, EVR116 with a hot ion cathode IMR 285 attached), resulting in a pressure of typically 136 Pa inside the GAS. For sputtering, a DC power of 40 W was supplied by the power source (Advanced Energy, MDX 500). Prior to every deposition, the target was cleaned and the NP growth was conditioned with a closed shutter for the time (at least 30 s) required to reach stable deposition conditions.

Sample characterization

Transmission Electron Microscopy (TEM) was used to investigate the nanostructure of the NP-decorated ZnO:Ag thin films using a Tecnai F30 G2 microscope (field emission gun, 300 kV) equipped with a Si(Li) EDX detector (EDAX system). TEM samples were prepared by scratching the nano-micro-columnar film containing the bimetallic clusters with a sharp knife and by subsequently transferring the resulting powder to a carbon lacey Cu grid by touching.

Analogous to previous works, for the electrical measurements, interdigitating Au electrodes were deposited by sputter deposition on top of the thin film.[22, 30] The gas sensing properties were measured as reported previously.[21, 31, 32] Throughout this study, a typical concentration of 100 ppm of the respective gas species was applied to the gas sensors. To account for the low gas response of AgAu/ZnO:Ag and ZnO:Ag sensors towards hydrogen gas, the concentration in this test scenario was raised to 1000 ppm. The gas sensing properties were studied in a typical range of operating temperatures between 200 °C and 350 °C. The electrical measurements were performed using a Keithley 2400 SourceMeter, controlled by a LabView program (National Instruments).[30]

X-ray photoelectron spectroscopy (XPS, Omicron Nano-Technology GmbH, Al-anode, 240W) was applied to investigate the chemical composition of the deposited NPs and nanocomposites. The C-1s line of adventitious carbon at roughly 285.0 eV was used for charge referencing of all recorded spectra. The software CasaXPS (version 2.3.16) was used to quantify the composition of the AgAu and AgPt alloy NPs. Micro-Raman studies were performed at room temperature with a WITec alpha 300 RA system in backscattering configuration. The Nd-YAG laser power at the laser position was less than 4 mW.[32]

Calculation details

Density functional theory (DFT) ~~simulations~~ calculations ~~o~~f~~n~~ the interaction of a number of VOCs and molecular hydrogen with the ZnO($10\bar{1}0$):Ag, Ag_5Au_5/ZnO($10\bar{1}0$):Ag and Ag_9Pt/ZnO($10\bar{1}0$):Ag decorated surfaces are also reported. All calculations were performed using the Vienna *ab-initio* simulation package (VASP).[33-36] The valence electronic states were expanded via a plane-wave basis set with a kinetic energy cut-off of 400 eV. The projector augmented wave (PAW) method[37, 38] was used to represent the interactions between the core (Au, Pt: [Xe] $4f^{14}$; Ag: [Kr]; Zn: [Ar]; O, C: [He]) and the valence electrons. For the H atoms, the electron was treated as valence. The method of Grimme with Becke-Johnson damping [D3-(BJ)][39, 40] was applied to improve the description of the long-range dispersion forces. The simulations were carried out using the Perdew, Burke, and Ernzerhof (PBE)[41] exchange-correlation functional within the generalised gradient approximation (GGA). An effective U_{eff} value of 6.0 eV[32, 42] was applied to the strongly correlated and localised Zn 3*d* electrons to enhance the description of their on-site Coulomb interactions.[43, 44] However, no Hubbard Hamiltonian was employed for either the transition metal dopant or cluster~~s~~ states, as they are already delocalised given their low concentration[45] and metallic properties, respectively. The structures were optimised using the conjugate-gradients technique and were considered converged when the forces on all ~~the~~ ions were less than 0.01 eV $Å^{-1}$. All calculations were spin-polarised to describe properly the unpaired electrons produced upon Zn(II) substitution by Ag(I).

The calculations of the insulating surfaces and isolated molecules were carried out sampling only the *Γ* point in the reciprocal space. However, the metallic phases were modelled using a *Γ*-centred Monkhorst-Pack mesh[46] with a maximum separation of 0.17 $Å^{-1}$ between k-points. The partial occupancies for the surfaces and isolated molecules were determined using the Gaussian smearing method,[47] with a width set at 0.05 eV. For the geometry optimisation of the metallic phases, the partial occupancies were simulated using the Methfessel-Paxton scheme order 1 with a smearing width of 0.10 eV. However, the tetrahedron method with Blöchl corrections was used for the static calculations of the metallic phases to simulate the magnetic and electronic properties and to obtain accurate total energies. These criteria allowed convergence of the total energy within 10^{-4} eV per atom.

Results and discussion

Morphological, structural and micro-Raman characterizations

SEM micrographs of pristine ZnO:Ag columnar thin films, as well as of nanocomposites decorated with AgAu and AgPt bimetalic alloy NPs, are depicted in **Figure 2**. The morphology of a typical pristine ZnO:Ag thin film after heat treatment at 650 °C for 2 h (**Figure~~s~~ 2a** and **2b**) consists of closely packed and partially interconnected grains. The diameter of these grains varies between 50 and 400 nm. SEM micrographs of ZnO:Ag columnar thin films, which were decorated with AgPt NPs, are displayed in **Figure~~s~~ 2c** and **2d**. The bimetallic AgPt NPs have a diameter ranging between 5 and 15 nm and are well distributed on the surface of the ZnO:Ag columnar thin film, without formation of percolating paths. However, due to the stochastic character of the deposition method, occasional agglomeration of small numbers of NPs are observed (see **Figure 2d**). The SEM micrographs of ZnO:Ag thin films decorated by AgAu NPs are shown in **Figure~~s~~ 2e** and **2f**. In this case, the deposited NPs exhibit

typical NP diameters between 3 nm and 18 nm (see **Figure 2f**). In both cases, for both AgPt and AgAu alloy NPs, the mean diameter is considerably smaller than the grain diameter of the ZnO:Ag thin film. These observed diameters, as well as the sparse deposition with occasional agglomerations, agrees well with a typical NP deposition via GAS well below the percolation threshold.[29]

Moreover, TEM experiments were conducted to investigate the nanostructure and verify the presence of alloy NPs. For example, **Figure 3a** depicts an overview image of an AgAu/ZnO:Ag nanocomposite. The electron diffraction (ED) pattern, recorded at the tip of the displayed AgAu/ZnO:Ag grain, provides information that the doped columnar grains grow as single crystals along the c-axis of the Wurtzite-type structure. Furthermore, the ED pattern exhibits weaker diffraction intensities distributed on rings with d-spacings corresponding to ZnO. The appearance of these rings is attributed to polycrystalline ZnO, which is partially adhered to the surface. High resolution TEM micrographs (see **Figure 3b**) show the presence of NPs with diameters in the range of 5-20 nm, which is in good agreement with the observations from the SEM micrographs of **Figure 2f**. These NPs seem to be loosely bound to the ZnO surface and do not show a systematic intergrowth structure. The Fourier transform of the matrix verifies the presence of a single crystalline ZnO (zone axis [100]) phase. Due to the similar crystal structures of Ag and Au, the composition of the NPs could not be distinguished between the pure metals or alloy (zone axis [110]). To verify the presence of AgAu NPs (or AgPt NPs), the nanocomposite was investigated by EDX elemental mapping (see **Figure 3c** or **Figure S2**, respectively). The EDX elemental map (**Figure 3c**) clearly shows that the locations of the high Ag signal and the high Au signal overlap, which indicates the presence of AgAu alloy NPs. For Ag and Pt in the AgPt/ZnO:Ag nanocomposite (**Figure S2**), a similar trend is observed. It is reported that Ag and Pt form a miscibility gap ranging roughly from 13 $\%_{at}$ to 98 $\%_{at}$, with respect to Pt content.[48, 49] However, phase separation could not be identified within the measuring limits of the microscope used (**Figure S2**). Considering that Pt content is about 12 $\%_{at}$ (see XPS studies below), it is reasonable to assume that a solid solution has formed.

Figure S1 shows the Raman spectra of the AgAu- and AgPt-decorated ZnO:Ag columnar films. For all samples, the two dominant peaks were observed at ~100 cm^{-1} and ~438 cm^{-1}, which are attributed to the E_2(low) and E_2(high) modes of the wurtzite structure of ZnO, respectively. Other peaks with lower intensities were observed at ~337, ~380, ~410, ~576 and ~584 cm^{-1}, which are attributed to E_2(high)-E_2(low), A_1(TO), E_1(TO), A_1(LO) and E_1(LO) modes, respectively.[23, 24]

XPS studies

The ZnO:Ag nanocolumnar thin film (as a reference layer), as well as the nanocomposites decorated with the AgPt and AgAu alloy NPs, were investigated by XPS. **Figure 4a** shows the overview spectra of the nanocomposites (AgAu: red line, AgPt: blue line) and the reference layer (magenta, bottom line). Based on the characteristic peaks of these spectra, the elemental composition is determined. The elements Zn, O, C and Au are detected in all spectra. The position of the line C-1s in **Figure 4b**, which was used for charge referencing, indicates atmospheric surface contamination from organic compounds, such as carbohydrates. The prominent signal of Zn and O is attributed to the ZnO base layer. The comparison of the O-1s high resolution spectra (**Figure 4b**) indicates a similar peak position and shape for the investigated nanocomposites as well as for the pristine substrate. Ag is detected in all three samples, but the corresponding signal is rather weak, especially for the ZnO:Ag base layer, which is attributed to the low doping concentration of Ag. A comparison of high resolution spectra of the Ag-3d, Au-4d and Pt-4d lines can be found in **Figure S3**. The signal is stronger in the case of the AgAu NPs and AgPt NPs decorated nanocomposites, but due to the intentionally low surface coverage of NP, the signal is still weak for a precise quantification.

For further investigation of the deposited NPs, the reference spectra of AgPt and AgAu alloy NPs (deposited on silicon wafer pieces) are compared in **Figures 4c** and **4d**. The overview spectra in **Figure 4c** indicates the presence of Si, Cr, O, C, Ag and Au or Pt for the AgAu and AgPt NPs, respectively. To quantify the composition of the alloy NPs, a detailed binding energy scan of the Ag-3d, Au-4d and Pt-4d lines from 382 eV to 313 eV is shown in **Figure 4d**. Additional peaks with an offset to lower binding energies (by roughly 10 eV) occur in the spectra, due to the use of a non-monochromated X-ray source. In case of the AgAu NPs, the offset peak from Ag-$3d_{5/2}$ overlaps with the Au-$4d_{3/2}$ line. Accordingly, the Au-4f line was used for the quantification of Au, which was estimated at 52$\%_{at}$ in the AgAu NPs. For the AgPt NPs, the relevant Ag-3d and Pt-4d lines are well separated and correspond to a Pt content of roughly 12$\%_{at}$. Considering the lower sputtering rate of Pt compared to Au (roughly 0.57 of Au) and the difference in target design (three Au wires for AgAu and one Pt wire for AgPt), the difference in concentration of Ag in the AgPt and AgAu NPs is expected.[26-29] The estimated composition of AgPt and AgAu NPs is presented in **Table S1** in the Supporting Information.

Gas sensing properties

Figure 5a shows the gas response of the pristine ZnO:Ag, AgPt/ZnO:Ag and AgAu/ZnO:Ag nanocomposites to hydrogen gas (H_2) and different VOCs vapors, including such as ethanol, acetone, *n*-butanol, 2-propanol and methanol, at an operating temperature of 250 °C. In a typical gas sensing experiment, the thin film sensor was exposed to a concentration of 100 ppm of each VOC or H_2. However, in the case of the ZnO:Ag and AgAu/ZnO:Ag columnar films, an H_2 concentration of 1000 ppm was used to underline the low sensitivity of these sensors towards H_2. A considerable increase of the response to VOC vapors was observed for the ZnO:Ag columnar films that were decorated with AgAu NPs. The gas response of the ZnO:Ag columnar films to 1000 ppm of hydrogen and 100 ppm of ethanol, acetone, *n*-butanol, 2-propanol and methanol is ~2.1, ~31, ~16.5, ~41, ~52.5 and ~31, respectively, while for AgAu/ZnO:Ag it is ~2, ~85, ~99, ~130.5, ~156.5 and ~140, respectively. Compared to the pristine ZnO:Ag thin film, the gas response of AgAu/ZnO:Ag to ethanol, acetone, *n*-butanol, 2-propanol and methanol was increased by factor of ~2.8, ~6, ~3.2, ~3 and ~4.5, respectively. The gas response values are also

considerably higher compared to those obtained for monometallic Ag NP-decorated ZnO:Ag columnar films synthesized by the same method,[50] proving the higher efficiency of bimetallic NP decoration. The low gas response to hydrogen gas is characteristic for all samples, with the exception of the AgPt/ZnO:Ag columnar films. Alt~~T~~though the decoration with the AgPt alloy NPs leads to a decrease in response for all the VOCs tested, by a factor of 2, it enhances the sensitivity to 100 ppm of H_2 gas by a factor 40. This is a large change compared to the almost no response to H_2 gas in the case of the reference and the AgAu-~~ –~~decorated sample sets, which ~~. This~~ indicates the possibility of tailoring the selectivity of ZnO:Ag thin film sensors by surface decoration with bimetallic NPs of different alloy systems. In addition to contemporary approaches, e.g. ~~like~~ incorporating molecular sieves, the versatility of GAS to produce a variety of metal, metal alloy and metal oxide NPs opens up a highly interesting research field for further improvements in sensor selectivity.

Figures 5b and **5c** show the dependence of the gas response to H_2 gas and different VOC vapors on the operating temperature for the AgPt/ZnO:Ag and AgAu/ZnO:Ag nanocomposites, respectively. In both cases, the optimal operating temperature is 250 - 300 °C. At operating temperatures lower than 200 °C no gas response higher than 1.5 was observed, and this temperature regime was therefore not investigated in detail any further.

The dynamic response of the AgPt/ZnO:Ag columnar films to 100 ppm of H_2 gas at different operating temperatures (200 – 350 °C) is presented in **Figure 6a**. The calculated values for the associated response and recovery times are presented in **Figure 6b**. The response times are confined to a small range (11 – 20 s), while the recovery times decrease from 36 s to 10 s when the operating temperature rises from 200 to 350 °C.

The dependence of the H_2 gas response (S_{H2}) to its concentration at 250 and 300 °C is presented in **Figure 6c.** A power law relationship is observed ($S_{H2} \propto p_{H2}^{\beta}$), where β is the slope of log S_{H2} *vs.* log p_{H2}.[32] $\beta \approx 0.85$ at both 250 and 300 °C. The theoretical detection limits calculated for the H_2 gas (criterion for gas detection: $I_{gas}/I_{air} > 1.2$ [51]) were ~1 and ~0.6 ppm at 250 and 300 °C, respectively.

The dynamic responses of the AgAu/ZnO:Ag columnar films to 100 ppm of VOC vapors at their optimal operating temperatures of 250 °C are presented in **Figure 6d**. All samples show fast signal recovery to the initial electrical baseline after evacuation of the vapors from the test chamber, which is essential for the reliability of sensors and their practical applications. The calculated response and recovery times versus the operating temperature are presented in **Table 1** and **Figure 6e**. The recovery times for all samples are comparable to one of the best results reported for functionalized/decorated ZnO samples (see **Table 2**).

Table 2 shows other results for high performance VOC vapors sensors based on ZnO micro- and nano-structures functionalized/decorated/modified with monometallic and bimetallic noble metals (Au, Ag, Pt). This table clearly demonstrates that our results are equivalent or superior ~~in comparison~~ to the performances reported for highly sensitive VOC sensors, although ~~.~~ ~~T~~there are several reports of H_2 response values much higher than for our AgPt/ZnO:Ag columnar films.[1, 5, 52-54] However, the remarkable point of our materials ~~in this case~~ is the possibility to change the selectivity from VOC vapors to H_2 gas, which opens the opportunity for the fabrication of highly selective gas sensors. In addition, the platinum content in the bimetallic AgPt NPs, which in this work was determined to be roughly 12%$_{at}$, results in a more cost-effective~~icient~~ approach to tailor the sensor selectivity compared to the use of the pure material.

The dependence of the gas response on the concentration of VOC vapors for the AgAu/ZnO:Ag columnar films is presented in **Figure 6f**. For ethanol, acetone, *n*-butanol, 2-propanol, and methanol the β value is ≈ 0.87, 0.88, 0.83, 0.82, and 0.78, respectively, whereas the estimated theoretical detection limit for ethanol, acetone, *n*-butanol, 2-propanol, and methanol are ~1, 0.8, 0.5, 0.4, 0.3 and 0.2 ppm, respectively.

Alloy NP-decorated thin film gas sensors as candidate materials for monitoring thermal runaway in Li-Ion-Batteries

From the gas sensing studies, it can be concluded that the surface decoration of the ZnO:Ag columnar films with AgAu NPs increases the selectivity to VOC vapors, while the surface decoration using AgPt NPs changes the response and leads to high selectivity to hydrogen gas. Thus, the selectivity of the ZnO:Ag films can be easily tuned using bimetallic NPs of different composition for surface decoration of the columns, which is of significant interest for gas sensing applications. In view of the versatility in tailoring the sensor's selectivity, and taking into account its fast response and recovery times, the alloy NP-decorated ZnO:Ag thin film sensors are highly promising materials for early hazard detection in LIBs, where many of the decomposition products, especially from the electrolyte solvents, are extremely flammable.[18, 20] Hazard detection in LIBs is especially demanding, as thermal runaway in a mal functioning cell can rapidly destroy the whole device and other neighboring devices, leading to a complete failure of all individual cells. For critical applications, e.g. in the automotive sector, each cell should be equipped with a fast and robust hazard detection system in order to prevent fire spreading to other cells.

In the case of thermal runaway, the LIB heats to over 200 °C and produces large amounts of H_2 gas. Applying the alloy NP/ZnO:Ag thin film sensors in close vicinity of each battery cell would allow the identification of failing units as the H_2 gas produced can be detected, whereas the thermal runaway provides the appropriate operating temperature for the sensor. Accordingly, the sensitivity of the AgPt/ZnO:Ag sensor towards H_2 would be enhanced as the temperature is raised, making this decorated surface an excellent material for the detection of thermal runaway in LIB. In contrast, the AgAu/ZnO:Ag sensor has a significantly lower response towards H_2 gas and is therefore an effective material to rule out sensor malfunction.

Thus, the integration of alloy NP/ZnO:Ag thin film sensors into individual battery cells is a potential pathway to achieve a cost effective and fast detection method of the early stages of thermal runaway, and to avoid the deterioration of other cells connected in parallel.

Commented [AV1]: Add here publication reference: 10.1021/acssensors.5b00236

Gas sensing mechanism for bimetallic alloy NP-decorated films

The gas sensing mechanism of the decorated columnar films can be explained by the electronic and chemical sensitization effects, i.e. the formation of nano-Schottky barriers at the interface between ZnO:Ag and the AgPt and AgAu alloy NPs,[2, 3, 55] as well as the catalytic properties of the bimetallic NPs. Given that the diameter of the ZnO:Ag grains is larger than its Debye length, the nano-Schottky barriers formed at the Au/ZnO:Ag and Pt/ZnO:Ag interface have a low impact on the improvement of the gas sensing properties.[5, 56] Moreover, since the AgPt and AgAu NP-decorated ZnO:Ag columnar films exhibit very different sensing properties, it can be concluded that the chemical sensitization effect (i.e. the catalytic properties of the bimetallic NPs) is the dominant effect. Choi *et al.* demonstrated that surface decoration of CuO NWs with different types of NPs, by modification of the conduction channel width, does not change the selectivity of the material.[56] Therefore, the key parameter that explains the selectivity change by surface decoration with AgPt NPs are the excellent catalytic properties of Pt with respect to hydrogen.[13] A number of studies have demonstrated that the addition of Pt NPs to different nano- and micro-structures of metal oxides can greatly enhance the response to H_2 gas.[13, 14, 57-59] The Pt NPs may provide more active sites than any other noble metal for the adsorption and catalytic dissociation of oxygen species and H_2 molecules.[13, 59] During the sensing process, the spillover and oxidation of hydrogen molecules by the adsorbed oxygen species (see **Eq. (1)**) located near the AgPt bimetallic NPs leads to a high response to H_2 gas.[14, 59] Taking into account the low concentration of roughly 12% of Pt in our bimetallic AgPt NPs, the strong shift of selectivity towards H_2 gas is even more remarkable .

$$2O^-_{(ads)} + 2H_2 \rightarrow 2H_2O + 2e^- \quad (1)$$

Liu *et al.* also observed that the addition of Pt NPs to SnO_2 leads to a considerable decrease in the response to VOC vapors, while the addition of Au NPs leads to the opposite effect.[13, 59] These findings also support the large effect of the chemical sensitization on the gas sensing properties and the selectivity of the AgPt/ZnO:Ag columnar films to H_2 gas. Another mechanism which can explain the high selectivity of the AgPt/ZnO:Ag samples is the formation of PtH_x species at the relatively high operating temperatures of 250 – 300 °C. Under these conditions, the number of hydrogen atoms per Pt atom increases, and the metal becomes a superior catalyst for hydride formation[14].

In the ~~case of~~ the AgAu/ZnO:Ag columnar films, the greatly enhanced sensing properties towards VOCs can be explained by the excellent catalytic properties of the Au component of the NPs towards~~for~~ the dissociation of oxygen and VOC molecules.[13, 59-62] The Au NPs will provide more active sites for the adsorption of oxygen species than the pristine surface of ZnO.[63] Many studies have demonstrated that the addition of Au NPs to nano- and micro-structures of metal oxides leads to an enhancement in the overall response and selectivity to VOC vapors.[60-64] The proposed reaction for the oxidation of the VOC molecules by the adsorbed oxygen species can be described as follows:[6, 63, 65-67]

$$CH_3COCH_3(acetone) + 8O^- \leftrightarrow 3CO_2 + 3H_2O + 8e^- \quad (2)$$

$$C_2H_5OH(ethanol) + 6O^- \leftrightarrow 2CO_2 + 3H_2O + 6e^- \quad (3)$$

$$CH_3OH(methanol) + O^- \leftrightarrow HCHO + H_2O + e^- \quad (4)$$

$$C_3H_7OH(2-propanol) + O^- \rightarrow (CH_3)_2CO(acetone) + H_2O + e^- \quad (5)$$

$$C_4H_9OH(n-butanol) + 12O^- \rightarrow 4CO_2 + 5H_2O + 12e^- \quad (6)$$

The high response to 2-propanol, compared to other VOC vapors, can be explained by the molecule possessing the largest number of (-CH_2) groups, which leads to its decomposition and oxidation occurring more easily.[68, 69] The general reaction can be described as:[70]

$$VOC + nO^- \rightarrow aCO_2 + bH_2O + ne^- \quad (7)$$

Calculated properties

Calculated properties

The DFT calculations have been performed to gain insight into the physio-chemical properties of the gas molecules (CH_3CH_2OH, CH_3COCH_3, *n*-C_4H_9OH, 2-C_3H_7OH, CH_3OH and H_2) adsorbed on the Ag-doped ZnO$(10\bar{1}0)$ surface decorated with Ag_5Au_5 and Ag_9Pt clusters. The aim of these calculations is to support experiment and explain the experimentally observed enhanced sensitivity and the change in selectivity reported for the systems studied.

Terminations *A* and *B* of the ZnO$(10\bar{1}0)$ surface were modelled using slabs with an area of 98.574 Å^2 and containing 96 atoms distributed in 8 atomic layers, see **Figure 7a**. A vacuum gap of 20 Å along the direction perpendicular to the surface is added to separate each slab from its periodic image. More details regarding the stacking of the layers, and a description of the surface terminations and the number of layers with the atoms frozen at their bulk positions can be found elsewhere.[42]

The substitutional doping of the ZnO $(10\bar{1}0)$ surface by Ag and its effect on the surface structure, energies, as well as on the electronic and magnetic properties are examined. One Zn atom is replaced in order to model the lowest Ag content value of 2.73 $\%_{wt}$, which is allowed by the size of our 48 formula unit (f.u.) computational cell. Despite modelling a dopant concentration almost threefold higher than the 0.95 $\%_{wt}$ used for the experiments, previous works have shown excellent agreement between the two approaches.[25, 42] The substitutional doping of the symmetrically inequivalent exposed Zn atoms was investigated, corresponding to the following solid state reaction,

$$Zn_{48}O_{48}(10\bar{1}0) + Ag(fcc) = Zn_{47}AgO_{48}(10\bar{1}0) + Zn(hcp) \quad (8)$$

Commented [AV2]: It looks like the "l" of isopropanol is outside of the brackets – could you please fix this?
The same holds for ethanol, acetone and methanol – in my version it lookslike the last letter is outside of the bracket.

Commented [AV3]: Please change here "tan" to be in italics. Unfortunately I cannot open the equation object in my word

Commented [AV4]: Ohh, here we have to be careful – unfortunately I did not notice it before.
2-propanol does not have any CH2 groups. It is "CH3-CHOH-CH3"
n-butanol has the highest number of CH2 groups (CH3-CH2-CH2-CH2OH)

Formatted: Indent: First line: 0 cm

Formatted: Font: Bold, Italic

where the face-centred cubic (*fcc*) Ag and hexagonal close-packed (*hcp*) Zn were modelled using the one- and two-atoms primitive unit cells, respectively.

The surface free energy (σ) of the partially decorated material has been estimated using,

$$\sigma = \gamma_r + \frac{E_{dop} - E_{pris} - E_{Ag} + E_{Zn}}{A} \quad (9)$$

where γ_r is the surface energy for the relaxed pristine ZnO $(10\bar{1}0)$ surface, E_{dop} is the energy of the Ag-doped ZnO $(10\bar{1}0)$ surface, E_{pris} is the energy of the pristine ZnO $(10\bar{1}0)$ surface, E_{Ag} is the energy of one atom in the bulk of *fcc* Ag and E_{Zn} is the energy of one atom in the bulk of *hcp* Zn. The γ_r values for the relaxed pristine ZnO $(10\bar{1}0)$ surface were taken from previous work,[12] and **Table S2** shows the close agreement between the experimental and simulated lattice parameters for Ag and Zn.

Table 3 displays the surface free energies for the Ag-doped systems, indicating that only termination *A* is slightly stabilised by 14–18 meV Å^{-2} with respect to its pristine parent structure. However, substitutional doping of termination *B*, and in particular of its 3-fold Zn site, lead to the most thermodynamically stable doped surfaces, although they are less favourable than the pristine parent plane. The simulations suggest that in both terminations, doping the most exposed undercoordinated cation positions is ~5 meV Å^{-2} more favourable than the substitution of the 4-fold sites . It was found that large in-plane displacements of approximately 1 Å for the atoms within the topmost layer account for the exothermic enthalpy during the insertion of Ag in termination *A*. Moreover, minor concomitant shifts of 0.15 Å towards the bulk are also observed for the sub-surface plane of Zn atoms and the surface layer of counter-anions. These horizontal and vertical atomic shifts are only allowed in the doped termination *A* due to the large interlayer spacing of 1.848 Å between the surface and sub-surface planes.[42] In contrast, the densest topmost layers of termination *B* experience negligible displacements, with the exception of the O atoms surrounding the 3- and 4-fold Ag dopants, which move by 0.43 and 0.15 Å, respectively.

~~The~~ Bader charge analysis[71-73] shows that Zn ions draw 58–60% of the electrons required to become neutral atoms from the Ag atoms, in agreement with their different charges in the pristine and doped surfaces, respectively. However, the largest electronic transfer is 68% ~~for the doping of~~ when the 3-fold position of termination *B* is doped, which is also the most stable surface of this study. We found different redox compensation mechanisms for the electronic deficit caused by ~~of~~ the replacement of the Zn atoms ~~leaving both~~in the two terminations of the ZnO $(10\bar{1}0)$ surface. In~~For~~ termination *A*, the 3-fold Zn ions provide an excess of electrons, which also reduces the exposed oxygen atoms by a further 0.1 e, thereby increasing the ionic character of the topmost surface layer. In~~For~~ termination *B*, the scenario for the charge compensation of Zn only involves the oxidation of its neighbouring oxygen atoms, as illustrated in **Figure 7b**. The charge density difference schemes were constructed by subtracting the sum of the electron charge densities of the clean surface and isolated dopant, with identical structure as in the doped form, from the electron density of the total system obtained from static ~~static~~ calculations. The simulation of the doped terminations *A* and *B* suggests that most atoms remain non-magnetic following the process represented in equation ~~(8)~~ (8). However, the Ag introduced alongside the 3-fold oxygen ions that directly coordinat~~eing~~ the dopant atoms become slightly magnetic at *ca* 0.3 μ_B per atom. From the small magnetic moment calculated for the dopant, an electronic distribution of $e_\uparrow^2 e_\downarrow^2 t_\uparrow^3 t_\downarrow^3$ has been inferred, corresponding to Ag^+ ions in a pseudo-tetrahedral crystal field of oxygen atoms.

The electronic properties of the doped surfaces were further investigated by measuring the work function (Φ) in order to gauge their reactivity as reducing agents.[25, 42] The work function is the energy needed to remove an electron from the Fermi level (E_F) of the surface into the electrostatic potential of the vacuum (V_V), calculated as $\Phi = V_V - E_F$. **Table 3** shows large reductions of over 50% in the work function values of all the doped surfaces with respect to their pristine counterparts of between 2.61 and 2.64 eV for the doped 4-fold position in both terminations. 2.61 and 2.64 eV for the doped 4-fold position in both terminations. However, for further analysis, we focus on the 3-fold doped slab of termination *B*, which possesses the lowest surface energy and is therefore likely to be the prominent plane exposed in the crystal morphology of ZnO.

Impregnation with Ag_5Au_5 and Ag_9Pt was also explored as a means to add decoration to the doped ZnO $(10\bar{1}0)$ surface and to reduce the detection limit of VOCs. Clusters composed of 10 atoms were chosen, as this is the smallest size to produce a close analogue to the experimental Ag content, i.e. 48% and 88%$_{at}$ in AgAu and AgPt NPs, respectively (cf. **Table S1**). The initial geometries for both noble bimetallic nanoclusters were derived from the *fcc* crystal structure common to the three monometallic materials[74-76] and the secondary Au or Pt element was placed at random crystallographic positions. **Table S2** illustrates the excellent agreement between the experimental and simulated lattice parameters for monometallic Au and Pt. Three different positions for the adsorption of the bimetallic clusters were chosen, *i.e.* (i) above, (ii) close to, and (iii) far away from the Ag dopant. Term $-(xE_{Ag} + yE_X)/A$ was added to equation (9), to evaluate the surface free energy of the fully decorated material; where X represents either *fcc* Au or Pt; E_X is the energy of one such atom in the bulk; x and y are the numbers of Ag and X atoms, respectively, in the cluster; E_{dop} becomes $E_{dop+clus}$, which is the energy of the Ag-doped ZnO $(10\bar{1}0)$ surface decorated with the NPs; while the remaining variables keep their previous definition. The simulations suggest that the addition of the bimetallic clusters increases the surface free energy with respect to the doped surface, particularly for the Pt-based particles, see **Table 4**. The most thermodynamically favourable adsorption position depends on the nature of the cluster, as Ag_5Au_5 is likely to sit far from the Ag dopant, while Ag_9Pt prefers a closer position.

The stability of the clusters on the surface was calculated using the adsorption energy (E_{ads}):

$$E_{\text{ads}} = E_{\text{dop+clus}} - E_{\text{dop}} - xE_{\text{Ag}} - yE_X \quad (10)$$

whose calculated values are in agreement with the trend in surface free energies for the Ag_5Au_5 clusters only, see **Table 4**. The lack of correlation between the adsorption energies of Ag_9Pt and their surface free energies can be explained based on the random position that Pt can adopt within the cluster during geometry optimisation. The positive values calculated for all the adsorption energies, which are largest for Ag_5Au_5, indicate that although these are thermodynamically unfavourable processes, the impregnated clusters are stable due to strong cohesive forces. Interestingly, the lowest adsorption energy values of 5.32 and 2.95 eV were calculated for the most stable adsorption position of the Au- and Pt-based NPs, respectively.

The incorporation of both nanoclusters slightly raises the work function of the fully decorated surfaces with respect to the doped system. The lowest work function is predicted for the facet containing the Ag_9Pt NP in the most favourable adsorption position. However, the largest value for this type of thermodynamic work was calculated for the surface decorated using the Ag_5Au_5 cluster in the most stable binding site. The small magnetic moments of the Ag dopant vanish after adsorption of the nanoclusters in any of the positions considered. Most of the adsorbed clusters are non-magnetic, but the simulations reveal a small mean value of 0.04 μ_B for each atom within the Ag_5Au_5 particles sited above and close to the dopant. Large positive charges of 1.4 e^- are located on the Ag atom of the cluster, while the secondary Au and Pt metals are reduced by −0.7 and −0.4 e^-, in agreement with their respective electronegativities. The net charge balance results in all noble bimetallic particles upon adsorption losing ~0.9 e^- to the Zn atoms underneath and the O ions near the dopant.

The adsorption of the single molecules onto the doped and NP-decorated ZnO $(10\bar{1}0)$ surfaces was also studied and it was found that all these processes release energy, see **Table 5**. The molecules were introduced in several orientations at 1.5 Å from the surface and were subsequently allowed to relax to their equilibrium adsorption geometries. The calculated adsorption energies on the Ag-doped surface are roughly −1.5 to −1.7 eV for all the alcohols, which subtly depends directly on their molar mass. However, the strength of binding is approximately 0.5 eV less favourable for CH_3COCH_3 than for the alcohols, owing togiven the different chemical nature of their carbonyl and hydroxyl functional groups. The simulations suggest that the non-polar H_2 molecule has the overall lowest adsorption energy at ~−1.0 eV. The introduction of the Ag_9Pt nanocluster reduces the energetic preference of the alcohols and ketone for the decorated surface by approximately 1.0 and 0.5 eV, respectively, compared to the doped system. The largest energy released at $E_{ads.}$ = −1.387 eV was found for the adsorption of H_2 on the Ag_9Pt/ZnO:Ag surface, indicating a change in selectivity in agreement with our experiments. The impregnation with Ag_5Au_5 NPs leads to larger adsorption energies and enhanced sensitivity towards the VOCs with respect to the Ag_9Pt/ZnO:Ag surface. Remarkably, the decreasing order of binding strength for the organic molecules is $E_{ads}(CH_3COCH_3) \approx E_{ads}(2\text{-}C_3H_7OH) \approx E_{ads}(C_2H_5OH) > E_{ads}(n\text{-}C_4H_9OH) \approx E_{ads}(CH_3OH)$, showing no dependence on the type of functional group. The binding energy of −0.070 eV for H_2 on Ag_5Au_5/ZnO:Ag is the lowest calculated in this study, which explains the lack of selectivity found in our experiments for this molecule.

It was found that aAll the VOCs adsorb molecularly on the doped as well as on the NP- decorated ZnO $(10\bar{1}0)$ surfaces, in line with previous reports.[25, 42] OnFor the doped surface, three adsorption positions relative to the Ag atom were tested, *i.e.* the molecules directly interacting with the defect, or as well as with its first orand second nearest Zn neighbours. In the case of the VOCs, the preferred mode involves direct coordination between the adsorbate oxygen and the exposed Ag or Zn atom at around 2.15 and 2.00 Å, respectively. The hydroxy group of the alcohols forms a short hydrogen- bond at the typicala distance of 1.39 to 1.53 Å with a surface 3-fold oxygen atom, as shown in **Figure 7c** for *n*-C_4H_9OH. Other configurations are at least 0.108 eV less favourable than the most stable binding modes, as they involvecomprise dissociative adsorptions or distorted hydrogen- bonds. For example, CH_3OH can dissociate the hydroxy hydrogen, which is donated to the closest oxygen from the coordinated Ag adsorption site. Moreover, *n*-C_4H_9OH can form hydrogen- bonds with the oxygens lying either closer or farther away from the coordinated Ag and Zn cation than in the most stable adsorption modes. The free rotation around the C−OH bond and weak dispersion forces allow the hydrocarbon fragment of the alcohols to orientate as close as possible to the surface foinr all the adsorption modes. On the other handIn contrast, the flat ketone molecule stays adsorbed in a canted configuration, given owing to the tetrahedral nature of the metallic coordination site and the trigonal geometry of the sp^2-hybridised carbonyl oxygen. Unsurprisingly, the H_2 molecule has both minor exothermic molecular and moderately exothermic dissociative adsorption modes. This molecule appears tilted and hovering at, 2.10 Å from any of the Zn sites and the closest 3-fold oxygen. H_2 also dissociates upon interaction with the AgO or OO pair sites. For the dissociative adsorption configurations, the hydrogen atoms sit at 1.63 Å from the Ag-dopant and at the usual O-H bond distance of 0.98 Å from the 3-fold oxygen.

The addition of Ag_9Pt changes the adsorption geometry of CH_3OH, which prefers to interact through its hydroxy H with the Pt at a distance of 2.30 Å, which increases by 0.38 Å for C_2H_5OH. However, the alcohols of higher molar mass, *i.e.* *n*-C_4H_9OH and 2-C_3H_7OH, instead coordinate to the Pt atom by their hydroxy O at an average distance of 2.37 Å. CH_3COCH_3 binds the Pt atom at 2.20 Å, which is the smallest value reported for any VOC interacting with the Ag_9Pt/ZnO:Ag surface. Different behaviours were calculated for the hydrocarbon radical of the VOCs, which lies more parallel to the surface for the low mass alcohols and the ketone than for *n*-C_4H_9OH and 2-C_3H_7OH. H_2 dissociates upon adsorption to the Pt site, with the H atoms separated by 2.16 Å, explaining the largest exothermic enthalpy for the interaction with the supported Ag_9Pt cluster, as shown in **Figure 7d**.

Shifting to the Ag_5Au_5 particle increases the number of interactions between the surface and the VOC molecules, justifying the larger adsorption energies with respect to the Ag_9Pt/ZnO:Ag surface. The DFT adsorption geometries indicate that 2-C_3H_7OH and C_2H_5OH form the dative bonds O−Ag and H−Au bonds at 2.40 and 2.62 Å, respectively, see **Figure 7e**. Furthermore, *n*-C_4H_9OH and CH_3OH have similar adsorption configurations asthan the alcohols of

intermediate molecular mass, but coordinate the Au atom at least 0.14 Å further away. CH_3COCH_3 can only form the O–Ag interaction at 2.30 Å, which is the shortest for the bimetallic Ag_5Au_5 cluster, as displayed in **Figure 7f**. Finally, the H_2 molecule stays perpendicular to the surface and 2.92 Å from the Au atom, leading to the smallest adsorption energy calculated for this molecule in this study.

Bader charge analysis shows that all VOCs become positively charged upon adsorption on the doped surface, with the largest transfer of 0.09 e^- obtained for the Ag site, as shown in **Table 5**. Charge donations decrease around 50% after introducing the Ag_9Pt cluster and the negative values calculated for the low molecular mass alcohols confirm their adsorption geometry via the hydroxy H. Electron transfers vanish for the molecules adsorbed on Ag_5Au_5, with the exception of the negatively charged *n*-C_4H_9OH and CH_3OH, which sit furthest away from the cluster. H_2 suffers the largest charge withdrawal reported for adsorptions on the doped surface, but it is predicted that the H–Zn hydrogen gains −0.20 e^- while the hydroxy H loses 0.64 e^-. The reverse direction of electron transport for the interaction with the bimetallic nanoclusters was observed, as H_2 gains a small electronic charge and remains molecular.

Conclusions

In summary, the surface of ZnO:Ag nanostructured columnar grains was successfully decorated with AgPt and AgAu bimetallic alloy NPs using a custom-made high vacuum deposition system with an in-house Haberland type Gas Aggregation Source. Gas sensing measurements were carried out to reveal the response of the thin films to H_2 gas and various VOC vapors. The underlying gas sensing mechanisms for the AgPt as well as AgAu NP-decorated ZnO:Ag thin films was proposed and discussed in terms of the electronic and chemical sensitization effect of the bimetallic alloy NPs.

The nanocomposites with AgAu NPs exhibit a highly improved response to VOC vapors compared to the pristine ZnO:Ag thin films and previously reported nanocomposites based on ZnO:Ag and Ag NPs. The gas response to 100 ppm of ethanol, acetone, *n*-butanol, 2-propanol and methanol vapors was increased by a factor of ~2.8, ~6, ~3.2, ~ 3 and ~4.5, respectively, compared to pristine ZnO:Ag thin films. In contrast, the nanocomposite decorated with the AgPt NPs shows a remarkable change in selectivity toward H_2 gas. While the response to all VOC vapors is considerably decreased once AgPt NPs are introduced on the surface of ZnO:Ag columnar films, the response to H_2 is increased by more than one order of magnitude.

The affinity of small molecules towards the doped and NP decorated ZnO $(10\bar{1}0)$ surfaces was also investigated computationally. ~~D~~The ~~d~~oping with Ag atoms was modelled, where ~~and~~ it was found that the most stable substitution occurs for the 3-fold Zn surface sites. Subsequently, Ag_9Pt and Ag_5Au_5 clusters prefer to bind the surface above and far away from the dopant atom, respectively. When studying the ~~The~~ adsorption of CH_3CH_2OH, CH_3COCH_3, *n*-C_4H_9OH, 2-C_3H_7OH, CH_3OH and~~,~~ H_2 on the doped surfaces and at the nanoclusters, ~~was also studied.~~ it was found that t~~T~~he VOCs release the largest and smallest energies upon adsorption to the doped surfaces and Ag_9Pt cluster, respectively, in agreement with the enhanced selectivity of the former. The dissociative adsorption of H_2 on the $Ag_9Pt/ZnO(10\bar{1}0)$:Ag surface causes ~~has~~ the largest calculated adsorption energy ~~calculated~~ for any of the NP-decorated surfaces, supporting the change in selectivity reported for this system.

We have shown that the decoration of ZnO:Ag columnar thin films with bimetallic NPs of noble metals provides a viable route to tailor the sensitivity as well as selectivity of ZnO:Ag gas sensors. It was found that AgAu NPs lead to high sensitivity as well as fast response and recovery times for the detection of the types of VOCs studied. In addition, the possibility to change the selectivity of ZnO:Ag thin films by surface decoration with bimetallic NPs is a feasible, effective and flexible approach for the fabrication of highly selective sensors.

Considering the low concentration of about 12%$_{at}$ of Pt in the AgPt bimetallic alloy NPs, this sensor is a promising prototype of a cost effective H_2 gas sensor for early hazard detection in lithium ion batteries. Given the high versatility and adaptability of the thin film fabrication process, in combination with the application of alloy NPs for surface decoration, the approach presented in this work offers significant potential for gas sensing applications, for example for the early detection of thermal runaway in LIB.

Conflicts of interest

There are no conflicts to declare.

Acknowledgements

Dr. Lupan acknowledges the Alexander von Humboldt Foundation for the research fellowship for experienced researchers 3-3MOL/1148833 STP at the Institute for Materials Science, Kiel University, Germany. This research was funded partially by the German Research Foundation (DFG) under ~~the~~ schemes SFB1261 and FOR2093 'Memristive devices for neuronal systems' as well as by the Federal Ministry of Education and Research in Germany under ~~the~~ project "PorSSi" (03XP0126 B). This research was partly supported by ~~the~~ project AMOXES. N.H.d.L., D.S.C. and A.C.E. ~~We~~ acknowledge the Engineering and Physical Sciences Research Council (EPSRC grant EP/K009567/2) for funding. *Via* their~~our~~ membership of the UK's HEC Materials Chemistry Consortium, which is funded by EPSRC (EP/L000202/1, EP/R029431/1), this work used the ARCHER UK National Supercomputing Service (https://www.archer.ac.uk). This work ~~was also~~ employed~~performed using~~ the computational facilities of the Advanced Research Computing @ Cardiff (ARCCA) Division, Cardiff University and ~~. This research was undertaken using~~ the Supercomputing Facilities at Cardiff University operated by ARCCA on behalf of the Cardiff Supercomputing Facility and the Supercomputing Wales (SCW) projects. We acknowledge the support of the latter, which is part-funded by the European

Regional Development Fund (ERDF) *via* Welsh Government. All data created during this research is openly available from ~~the~~ Cardiff University~~'s's~~ Research Portal at http://doi.org/10.17035/d.2019.0081500252.

Author Contributions

A.V., V.P., and O.L. synthesized the AgAu and AgPt bimetallic alloy NPs -functionalized ZnO:Ag nanomaterial. O.L. developed synthesis from chemical solution procedure SCS for ZnO. A.V. and F.F. developed functionalization procedure for AgAu and AgPt bimetallic alloy NPs, set-up and realized all experiments and XPS analysis. O.L., V.P., A.V., M.I.T., M.H., H.C. and S.N. adapted technological approach for material synthesis and integration/fabrication of the sensors for early hazard detection in batteries. V.P. and O.L. carried out the measurement of sensing properties of sensors based on such structures and analyzed data. T.D., N.W. and L.K. performed TEM studies and analysis. V.P., O.L., S.N., R.A., M.I.T. and H.C. analyzed the results, including experimental data and revised draft. N.H.d.L., D.S.C. and A.C.E. realized the computational part and revised draft. A.V., P.V., D.S.C., S.N., T.D., N.W. and O.L. prepared the manuscript draft. O.L., A.V., F.F., L.K., S.N. and R.A. conducted study conception and design and final approval of the version to be published. All authors reviewed the manuscript.

References

1. O. Lupan, V. Postica, F. Labat, I. Ciofini, T. Pauporté and R. Adelung, Ultra-Sensitive and Selective Hydrogen Nanosensor With Fast Response at Room Temperature Based on a Single Pd/ZnO Nanowire, *Sens. Actuators, B*, 2018, **254**, 1259-1270.
2. A. Kolmakov, D. O. Klenov, Y. Lilach, S. Stemmer and M. Moskovits, Enhanced Gas Sensing by Individual SnO_2 Nanowires and Nanobelts Functionalized with Pd Catalyst Particles, *Nano Lett.*, 2005, **5**, 667-673.
3. N. Yamazoe, New approaches for improving semiconductor gas sensors, *Sens. Actuators, B*, 1991, **5**, 7-19.
4. S.-S. Chen, X.-X. Lin, A.-J. Wang, H. Huang and J.-J. Feng, Facile synthesis of multi-branched AgPt alloyed nanoflowers and their excellent applications in surface enhanced Raman scattering, *Sens. Actuators B*, 2017, **248**, 214-222.
5. O. Lupan, V. Postica, R. Adelung, F. Labat, I. Ciofini, U. Schürmann, L. Kienle, L. Chow, B. Viana and T. Pauporté, Functionalized Pd/ZnO Nanowires for Nanosensors, *Phys. Status Solidi RRL*, 2017, **12**, 1700321.
6. J. Guo, J. Zhang, M. Zhu, D. Ju, H. Xu and B. Cao, High-performance gas sensor based on ZnO nanowires functionalized by Au nanoparticles, *Sens. Actuators B*, 2014, **199**, 339-345.
7. S. M. Majhi, P. Rai and Y.-T. Yu, Facile Approach to Synthesize Au@ZnO Core–Shell Nanoparticles and Their Application for Highly Sensitive and Selective Gas Sensors, *ACS Appl. Mater. Interfaces*, 2015, **7**, 9462-9468.
8. O. Lupan, V. Postica, N. Wolff, J. Su, F. Labat, I. Ciofini, H. Cavers, R. Adelung, O. Polonskyi, F. Faupel, L. Kienle, B. Viana and T. Pauporté, Low-Temperature Solution Synthesis of Au-Modified ZnO Nanowires for Highly Efficient Hydrogen Nanosensors, *ACS Appl. Mater. Interfaces*, 2019, **11**, 32115-32126.
9. J. P. V. Damasceno, C. M. Maroneze, M. Strauss, F. A. Sigoli and I. O. Mazali, Preparation of supported AuPd nanoalloys mediated by ionic liquid-like functionalized SBA-15: structural correlations concerning its catalytic activity, *New J. Chem.*, 2016, **40**, 6636-6642.
10. Y. Yong, C. Li, X. Li, T. Li, H. Cui and S. Lv, Ag_7Au_6 Cluster as a Potential Gas Sensor for CO, HCN, and NO Detection, *J. Phys. Chem. C*, 2015, **119**, 7534-7540.
11. S.-J. Kim, S.-J. Choi, J.-S. Jang, H.-J. Cho, W.-T. Koo, H. L. Tuller and I.-D. Kim, Exceptional High-Performance of Pt-Based Bimetallic Catalysts for Exclusive Detection of Exhaled Biomarkers, *Adv. Mater.*, 2017, **29**, 1700737.
12. S.-W. Choi, A. Katoch, G.-J. Sun and S. S. Kim, Bimetallic Pd/Pt nanoparticle-functionalized SnO_2 nanowires for fast response and recovery to NO_2, *Sens. Actuators B*, 2013, **181**, 446-453.
13. F. Fan, J. Zhang, J. Li, N. Zhang, R. Hong, X. Deng, P. Tang and D. Li, Hydrogen sensing properties of Pt-Au bimetallic nanoparticles loaded on ZnO nanorods, *Sens. Actuators B*, 2017, **241**, 895-903.
14. K. Hassan and G.-S. Chung, Catalytically activated quantum-size Pt/Pd bimetallic core–shell nanoparticles decorated on ZnO nanorod clusters for accelerated hydrogen gas detection, *Sens. Actuators B*, 2017, **239**, 824-833.
15. T. Shiravand and A. Azadbakht, Impedimetric biosensor based on bimetallic AgPt nanoparticle-decorated carbon nanotubes as highly conductive film surface, *J. Solid State Electrochem.*, 2017, **21**, 1699-1711.
16. K. K. Haldar, S. Kundu and A. Patra, Core-Size-Dependent Catalytic Properties of Bimetallic Au/Ag Core–Shell Nanoparticles, *ACS Appl. Mater. Interfaces*, 2014, **6**, 21946-21953.
17. Z. Y. Li, J. P. Wilcoxon, F. Yin, Y. Chen, R. E. Palmer and R. L. Johnston, Structures and optical properties of 4-5 nm bimetallic AgAu nanoparticles, *Faraday Discuss.*, 2008, **138**, 363-373.
18. M. Metzger, B. Strehle, S. Solchenbach and H. A. Gasteiger, Origin of H_2 Evolution in LIBs: H_2O Reduction vs. Electrolyte Oxidation, *J. Electrochem. Soc.*, 2016, **163**, A798-A809.
19. D. Ortiz, V. Steinmetz, D. Durand, S. Legand, V. Dauvois, P. Maître and S. Le Caër, Radiolysis as a solution for accelerated ageing studies of electrolytes in Lithium-ion batteries, *Nature Commun.*, 2015, **6**, 6950.
20. A. W. Golubkov, D. Fuchs, J. Wagner, H. Wiltsche, C. Stangl, G. Fauler, G. Voitic, A. Thaler and V. Hacker, Thermal-runaway experiments on consumer Li-ion batteries with metal-oxide and olivin-type cathodes, *RSC Adv.*, 2014, **4**, 3633-3642.
21. V. Postica, I. Hölken, V. Schneider, V. Kaidas, O. Polonskyi, V. Cretu, I. Tiginyanu, F. Faupel, R. Adelung and O. Lupan, Multifunctional device based on ZnO:Fe nanostructured films with enhanced UV and ultra-fast ethanol vapour sensing, *Mater. Sci. Semicond. Proc.*, 2016, **49**, 20-33.
22. J. Gröttrup, V. Postica, N. Ababii, O. Lupan, C. Zamponi, D. Meyners, Y. K. Mishra, V. Sontea, I. Tiginyanu and R.

Adelung, Size-Dependent UV and Gas Sensing Response of Individual Fe_2O_3-ZnO:Fe Micro- and Nanowire Based Devices, *J. Alloys Compd.*, 2017, **701**, 920-925.

23. O. Lupan, L. Chow, S. Shishiyanu, E. Monaico, T. Shishiyanu, V. Şontea, B. Roldan Cuenya, A. Naitabdi, S. Park and A. Schulte, Nanostructured zinc oxide films synthesized by successive chemical solution deposition for gas sensor applications, *Mater. Res. Bull.*, 2009, **44**, 63-69.
24. O. Lupan, S. Shishiyanu, V. Ursaki, H. Khallaf, L. Chow, T. Shishiyanu, V. Sontea, E. Monaico and S. Railean, Synthesis of nanostructured Al-doped zinc oxide films on Si for solar cells applications, *Sol. Energy Mater. Sol. Cells*, 2009, **93**, 1417-1422.
25. V. Postica, A. Vahl, D. Santos-Carballal, T. Dankwort, L. Kienle, M. Hoppe, A. Cadi-Essadek, N. H. de Leeuw, M.-I. Terasa, R. Adelung, F. Faupel and O. Lupan, Tuning ZnO Sensors Reactivity toward Volatile Organic Compounds via Ag Doping and Nanoparticle Functionalization, *ACS Appl. Mater. Interfaces*, 2019, **11**, 31452-31466.
26. O. Polonskyi, T. Peter, A. Mohammad Ahadi, A. Hinz, T. Strunskus, V. Zaporojtchenko, H. Biederman and F. Faupel, Huge increase in gas phase nanoparticle generation by pulsed direct current sputtering in a reactive gas admixture, *Appl. Phys. Lett.*, 2013, **103**, 033118.
27. H. Haberland, M. Karrais, M. Mall and Y. Thurner, Thin films from energetic cluster impact: A feasibility study, *J. Vac. Sci. Technol., A*, 1992, **10**, 3266-3271.
28. P. Solař, O. Polonskyi, A. Olbricht, A. Hinz, A. Shelemin, O. Kylián, A. Choukourov, F. Faupel and H. Biederman, Single-step generation of metal-plasma polymer multicore@shell nanoparticles from the gas phase, *Sci. Rep.*, 2017, **7**, 8514.
29. A. Vahl, J. Strobel, W. Reichstein, O. Polonskyi, T. Strunskus, L. Kienle and F. Faupel, Single target sputter deposition of alloy nanoparticles with adjustable composition via a gas aggregation cluster source, *Nanotechnol.*, 2017, **28**, 175703.
30. O. Lupan, V. Postica, M. Mecklenburg, K. Schulte, Y. K. Mishra, B. Fiedler and R. Adelung, Low powered, tunable and ultra-light aerographite sensor for climate relevant gas monitoring, *J. Mater. Chem. A*, 2016, **4**, 16723-16730.
31. O. Lupan, V. Cretu, V. Postica, N. Ababii, O. Polonskyi, V. Kaidas, F. Schütt, Y. K. Mishra, E. Monaico, I. Tiginyanu, V. Sontea, T. Strunskus, F. Faupel and R. Adelung, Enhanced ethanol vapour sensing performances of copper oxide nanocrystals with mixed phases, *Sens. Actuators, B*, 2016, **224**, 434-448.
32. V. Cretu, V. Postica, A. K. Mishra, M. Hoppe, I. Tiginyanu, Y. K. Mishra, L. Chow, N. H. de Leeuw, R. Adelung and O. Lupan, Synthesis, characterization and DFT studies of zinc-doped copper oxide nanocrystals for gas sensing applications, *J. Mater. Chem. A*, 2016, **4**, 6527-6539.
33. G. Kresse and J. Hafner, Ab initio molecular dynamics for liquid metals, *Phys. Rev. B*, 1993, **47**, 558-561.
34. G. Kresse and J. Hafner, Ab initio molecular-dynamics simulation of the liquid-metal--amorphous-semiconductor transition in germanium, *Phys. Rev. B*, 1994, **49**, 14251-14269.
35. G. Kresse and J. Furthmüller, Efficient iterative schemes for ab initio total-energy calculations using a plane-wave basis set, *Phys. Rev. B*, 1996, **54**, 11169-11186.
36. G. Kresse and J. Furthmüller, Efficiency of ab-initio total energy calculations for metals and semiconductors using a plane-wave basis set, *Comput. Mater. Sci.*, 1996, **6**, 15-50.
37. P. E. Blöchl, Projector augmented-wave method, *Phys. Rev. B*, 1994, **50**, 17953-17979.
38. G. Kresse and D. Joubert, From ultrasoft pseudopotentials to the projector augmented-wave method, *Phys. Rev. B*, 1999, **59**, 1758-1775.
39. S. Grimme, J. Antony, S. Ehrlich and H. Krieg, A consistent and accurate ab initio parametrization of density functional dispersion correction (DFT-D) for the 94 elements H-Pu, *J. Chem. Phys.*, 2010, **132**, 154104.
40. S. Grimme, S. Ehrlich and L. Goerigk, Effect of the damping function in dispersion corrected density functional theory, *J. Comput. Chem.*, 2011, **32**, 1456-1465.
41. J. P. Perdew, K. Burke and M. Ernzerhof, Generalized Gradient Approximation Made Simple, *Phys. Rev. Lett.*, 1996, **77**, 3865-3868.
42. V. Postica, A. Vahl, J. Strobel, D. Santos-Carballal, O. Lupan, A. Cadi-Essadek, N. H. de Leeuw, F. Schütt, O. Polonskyi, T. Strunskus, M. Baum, L. Kienle, R. Adelung and F. Faupel, Tuning doping and surface functionalization of columnar oxide films for volatile organic compound sensing: experiments and theory, *J. Mater. Chem. A*, 2018, **6**, 23669-23682.
43. V. I. Anisimov, M. A. Korotin, J. Zaanen and O. K. Andersen, Spin bags, polarons, and impurity potentials in $La_{2-x}Sr_xCuO_4$ from first principles, *Phys. Rev. Lett.*, 1992, **68**, 345-348.
44. S. L. Dudarev, G. A. Botton, S. Y. Savrasov, C. J. Humphreys and A. P. Sutton, Electron-energy-loss spectra and the structural stability of nickel oxide: An LSDA+U study, *Phys. Rev. B*, 1998, **57**, 1505-1509.
45. D. O. Scanlon, B. J. Morgan and G. W. Watson, The origin of the enhanced oxygen storage capacity of $Ce_{1-x}(Pd/Pt)_xO_2$, *Phys. Chem. Chem. Phys.*, 2011, **13**, 4279-4284.
46. H. J. Monkhorst and J. D. Pack, Special points for Brillouin-zone integrations, *Phys. Rev. B*, 1976, **13**, 5188-5192.
47. N. D. Mermin, Thermal Properties of the Inhomogeneous Electron Gas, *Phys. Rev.*, 1965, **137**, A1441-A1443.
48. H. Okamoto, Ag-Pt (silver-platinum), *J. Phase Equilib.*, 1997, **18**, 485.
49. G. L. W. Hart, L. J. Nelson, R. R. Vanfleet, B. J. Campbell, M. H. F. Sluiter, J. H. Neethling, E. J. Olivier, S. Allies, C. I. Lang, B. Meredig and C. Wolverton, Revisiting the revised Ag-Pt phase diagram, *Acta Mater.*, 2017, **124**, 325-332.
50. O. Lupan, V. Postica, … and R. Adelung, Ag-doped and Ag-functionalized ZnO nanostructured films for VOCs sensing, *In Progress*, 2018, DOI: 10.1039/C6TA05347E.
51. I.-S. Hwang, S.-J. Kim, J.-K. Choi, J.-J. Jung, D. J. Yoo, K.-Y. Dong, B.-K. Ju and J.-H. Lee, Large-scale fabrication of highly sensitive SnO_2 nanowire network gas sensors by single step vapor phase growth, *Sens. Actuators B*, 2012, **165**, 97-103.
52. J. J. Hassan, M. A. Mahdi, C. W. Chin, H. Abu-Hassan and Z. Hassan, A high-sensitivity room-temperature hydrogen gas sensor based on oblique and vertical ZnO nanorod arrays, *Sens. Actuators B*, 2013, **176**, 360-367.
53. A. Katoch, S.-W. Choi, H. W. Kim and S. S. Kim, Highly sensitive and selective H_2 sensing by ZnO nanofibers and the underlying sensing mechanism, *J. Hazardous Mater.*, 2015, **286**, 229-235.

54. A. Katoch, Z. U. Abideen, H. W. Kim and S. S. Kim, Grain-Size-Tuned Highly H_2-Selective Chemiresistive Sensors Based on ZnO–SnO_2 Composite Nanofibers, *ACS Appl. Mater. Interfaces*, 2016, **8**, 2486-2494.
55. R.-J. Wu, D.-J. Lin, M.-R. Yu, M. H. Chen and H.-F. Lai, Ag@SnO_2 core–shell material for use in fast-response ethanol sensor at room operating temperature, *Sens. Actuators, B*, 2013, **178**, 185-191.
56. S.-W. Choi, A. Katoch, J.-H. Kim and S. S. Kim, Remarkable Improvement of Gas-Sensing Abilities in p-type Oxide Nanowires by Local Modification of the Hole-Accumulation Layer, *ACS Appl. Mater. Interfaces*, 2015, **7**, 647-652.
57. C. S. Rout, A. R. Raju, A. Govindaraj and C. N. R. Rao, Hydrogen sensors based on ZnO nanoparticles, *Solid State Commun.*, 2006, **138**, 136-138.
58. L. F. Zhu, J. C. She, J. Y. Luo, S. Z. Deng, J. Chen and N. S. Xu, Study of Physical and Chemical Processes of H_2 Sensing of Pt-Coated WO_3 Nanowire Films, *J. Phys. Chem. C*, 2010, **114**, 15504-15509.
59. C. Liu, Q. Kuang, Z. Xie and L. Zheng, The effect of noble metal (Au, Pd and Pt) nanoparticles on the gas sensing performance of SnO_2-based sensors: a case study on the {221} high-index faceted SnO_2 octahedra, *CrystEngComm*, 2015, **17**, 6308-6313.
60. W. Xia, C. Mei, X. Zeng, G. Fan, J. Lu, X. Meng and X. Shen, Nanoplate-Built ZnO Hollow Microspheres Decorated with Gold Nanoparticles and Their Enhanced Photocatalytic and Gas-Sensing Properties, *ACS Appl. Mater. Interfaces*, 2015, **7**, 11824-11832.
61. A. L. Zou, Y. Qiu, J. J. Yu, B. Yin, G. Y. Cao, H. Q. Zhang and L. Z. Hu, Ethanol sensing with Au-modified ZnO microwires, *Sens. Actuators B*, 2016, **227**, 65-72.
62. X.-j. Wang, W. Wang and Y.-L. Liu, Enhanced acetone sensing performance of Au nanoparticles functionalized flower-like ZnO, *Sens. Actuators B*, 2012, **168**, 39-45.
63. X. Li, X. Zhou, H. Guo, C. Wang, J. Liu, P. Sun, F. Liu and G. Lu, Design of Au@ZnO Yolk–Shell Nanospheres with Enhanced Gas Sensing Properties, *ACS Appl. Mater. Interfaces*, 2014, **6**, 18661-18667.
64. X. Liu, J. Zhang, L. Wang, T. Yang, X. Guo, S. Wu and S. Wang, 3D hierarchically porous ZnO structures and their functionalization by Au nanoparticles for gas sensors, *J. Mater. Chem.*, 2011, **21**, 349-356.
65. W. Tang, J. Wang, P. Yao and X. Li, Hollow hierarchical SnO_2-ZnO composite nanofibers with heterostructure based on electrospinning method for detecting methanol, *Sens. Actuators B*, 2014, **192**, 543-549.
66. S. Wlodek, K. Colbow and F. Consadori, Signal-shape analysis of a thermally cycled tin-oxide gas sensor, *Sens. Actuators B*, 1991, **3**, 63-68.
67. Y. Wang, B. Zhang, J. Liu, Q. Yang, X. Cui, Y. Gao, X. Chuai, F. Liu, P. Sun, X. Liang, Y. Sun and G. Lu, Au-loaded mesoporous WO_3: Preparation and n-butanol sensing performances, *Sens. Actuators B*, 2016, **236**, 67-76.
68. K. Arshak and I. Gaidan, Development of a novel gas sensor based on oxide thick films, *Mater. Sci. Eng. B*, 2005, **118**, 44-49.
69. M. Rafiqul Islam, N. Kumazawa and M. Takeuchi, Titaniumdioxide chemical sensor working with AC voltage, *Sens. Actuators B*, 1998, **46**, 114-119.
70. Z. Feng, Y. Ma, V. Natarajan, Q. Zhao, X. Ma and J. Zhan, In-situ generation of highly dispersed Au nanoparticles on porous ZnO nanoplates via ion exchange from hydrozincite for VOCs gas sensing, *Sens. Actuators B*, 2018, **255**, 884-890.
71. G. Henkelman, A. Arnaldsson and H. Jónsson, A fast and robust algorithm for Bader decomposition of charge density, *Comput. Mater. Sci.*, 2006, **36**, 354-360.
72. E. Sanville, S. D. Kenny, R. Smith and G. Henkelman, Improved grid-based algorithm for Bader charge allocation, *J. Comput. Chem.*, 2007, **28**, 899-908.
73. W. Tang, E. Sanville and G. Henkelman, A grid-based Bader analysis algorithm without lattice bias, *J. Phys.: Condens. Matter*, 2009, **21**, 084204.
74. K. H. Hong, G. M. McNally, M. Coduri and J. P. Attfield, Synthesis, Crystal Structure, and Magnetic Properties of $MnFe_3O_5$, *J. Inorg. Gen. Chem.*, 2016, **642**, 1355-1358.
75. L. P. Salamakha, E. Bauer, S. I. Mudryi, A. P. Gonçalves, M. Almeida and H. Noël, Isothermal section of the Ce–Au–Sb system at 870K, *J. Alloys Compd.*, 2009, **479**, 184-188.
76. Y. Chen, Y. Wei, P. Chang and L. Ye, Morphology-controlled synthesis of monodisperse silver spheres via a solvothermal method, *J. Alloys Compd.*, 2011, **509**, 5381-5387.
77. N. L. Tarwal, A. V. Rajgure, J. Y. Patil, M. S. Khandekar, S. S. Suryavanshi, P. S. Patil, M. G. Gang, J. H. Kim and J. H. Jang, A selective ethanol gas sensor based on spray-derived Ag–ZnO thin films, *J. Mater. Sci.*, 2013, **48**, 7274-7282.
78. Y. Wei, X. Wang, G. Yi, L. Zhou, J. Cao, G. Sun, Z. Chen, H. Bala and Z. Zhang, Hydrothermal synthesis of Ag modified ZnO nanorods and their enhanced ethanol-sensing properties, *Mater. Sci. Semicond. Proc.*, 2018, **75**, 327-333.
79. J. Ding, J. Zhu, P. Yao, J. Li, H. Bi and X. Wang, Synthesis of ZnO–Ag hybrids and their gas-sensing performance toward ethanol, *Ind. Eng. Chem. Res.*, 2015, **54**, 8947-8953.
80. Q. Xiang, G. Meng, Y. Zhang, J. Xu, P. Xu, Q. Pan and W. Yu, Ag nanoparticle embedded-ZnO nanorods synthesized via a photochemical method and its gas-sensing properties, *Sens. Actuators, B*, 2010, **143**, 635-640.
81. X. Xing, X. Xiao, L. Wang and Y. Wang, Highly sensitive formaldehyde gas sensor based on hierarchically porous Ag-loaded ZnO heterojunction nanocomposites, *Sens. Actuators, B*, 2017, **247**, 797-806.
82. N. Hongsith, C. Viriyaworasakul, P. Mangkorntong, N. Mangkorntong and S. Choopun, Ethanol sensor based on ZnO and Au-doped ZnO nanowires, *Ceram. Int.*, 2008, **34**, 823-826.
83. L. Chengchao, L. Limiao, D. Zhifeng, Y. Hongchun, X. Yingying, L. Yuan, C. Yong and W. Taihong, Rapid and ultrahigh ethanol sensing based on Au-coated ZnO nanorods, *Nanotechnol.*, 2008, **19**, 035501.
84. E. Wongrat, P. Pimpang and S. Choopun, Comparative study of ethanol sensor based on gold nanoparticles: ZnO nanostructure and gold: ZnO nanostructure, *Appl. Surf. Sci.*, 2009, **256**, 968-971.
85. J. Zhang, X. Liu, S. Wu, B. Cao and S. Zheng, One-pot synthesis of Au-supported ZnO nanoplates with enhanced gas sensor performance, *Sens. Actuators B*, 2012, **169**, 61-66.
86. T. Santhaveesuk, D. Wongratanaphisan and S. Choopun, Enhancement of sensor response by TiO_2 mixing and Au coating on ZnO tetrapod sensor, *Sens. Actuators B*, 2010, **147**, 502-507.

87. Z. Yuan, X. Jiaqiang, X. Pengcheng, Z. Yongheng, C. Xuedong and Y. Weijun, Decoration of ZnO nanowires with Pt nanoparticles and their improved gas sensing and photocatalytic performance, *Nanotechnol.*, 2010, **21**, 285501.

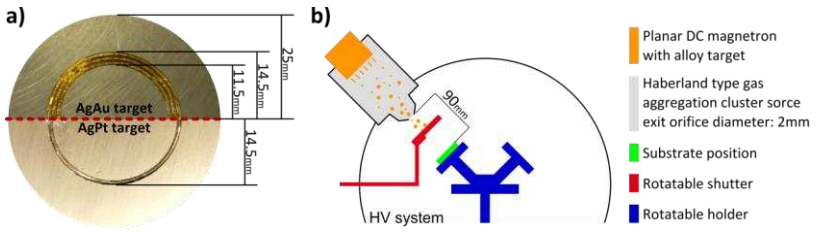

Figure 1. (a) Photographic image of the AgAu (top half) and AgPt (bottom half) composite targets; (b) Schematic illustration of the custom-built HV deposition system for bimetallic alloy NP deposition.

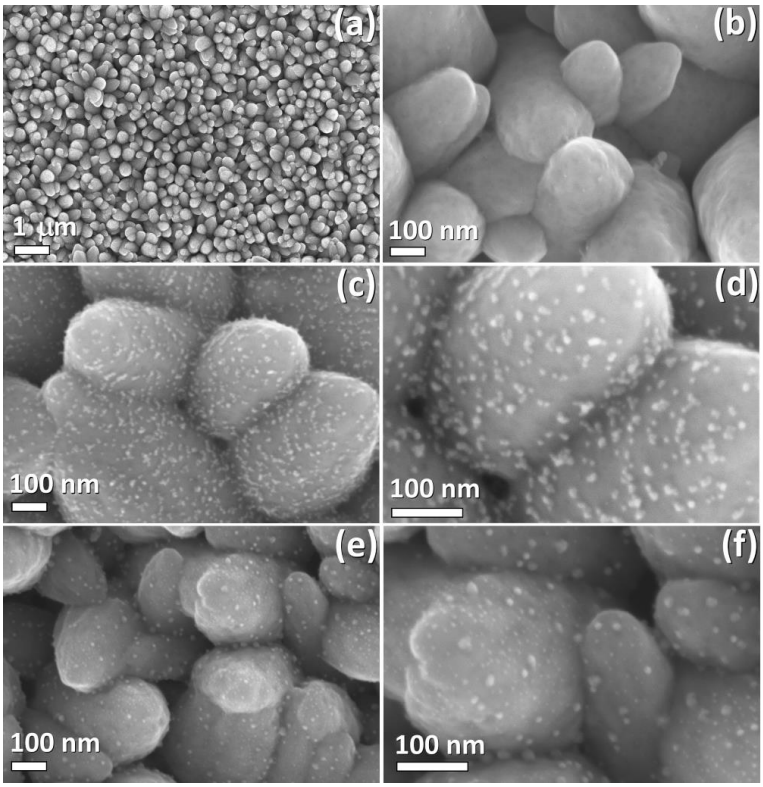

Figure 2. SEM micrographs of ZnO:Ag columnar thin films after thermal annealing at 650 °C for 2 h: (a,b) pristine ZnO:Ag thin films; (c,d) ZnO:Ag thin films decorated by AgPt NPs; (d,e) ZnO:Ag thin films decorated by AgAu NPs.

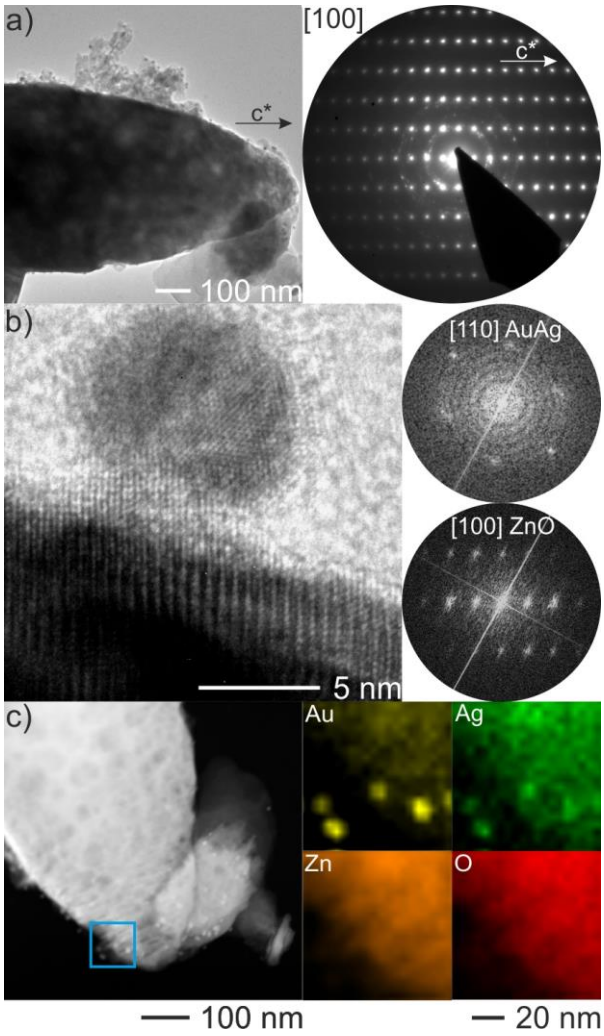

Figure 3. (a) Overview TEM micrograph of a AgAu/ZnO:Ag nanocomposite: Electron diffraction pattern of the tip of the AgAu/ZnO:Ag nanostructure verify that these are single crystalline structures and exhibit a *c*-axis growth direction. (b) HRTEM of a AgAu NP attached to the surface of the AgAu/ZnO:Ag nanostructure and corresponding FFT. (c) EDX elemental mapping of the marked region indicates the presence of AgAu alloy NPs.

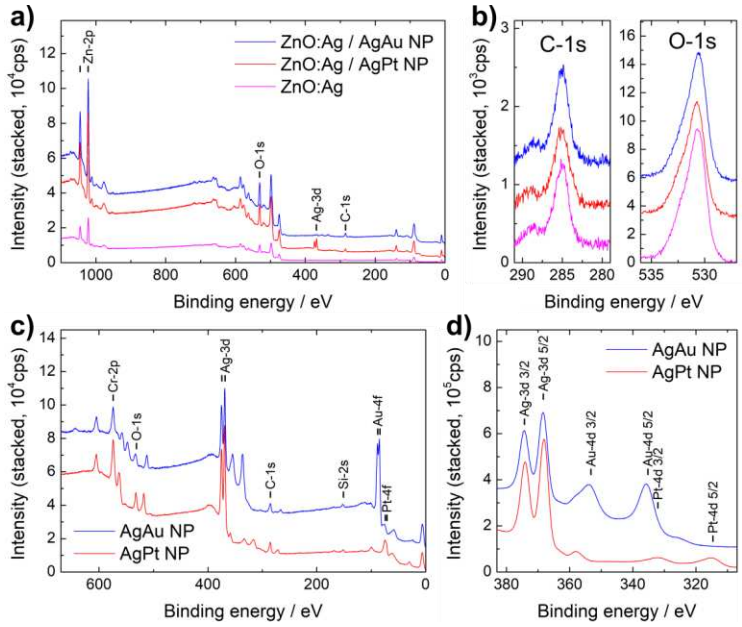

Figure 4. (a) Overview XPS spectra of ZnO:Ag columnar thin film (magenta line) and nanocomposites with AgAu (blue line) and AgPt (red line) bimetallic alloy NPs; (b) high resolution spectra of C-1s and O-1s lines; XPS spectra of AgAu alloy NP layers (blue line) and AgPt (red line) for overview (c); and detailed quantification of NP composition (d).

Commented [AV5]: could we please add "250°C" to figure (a)?

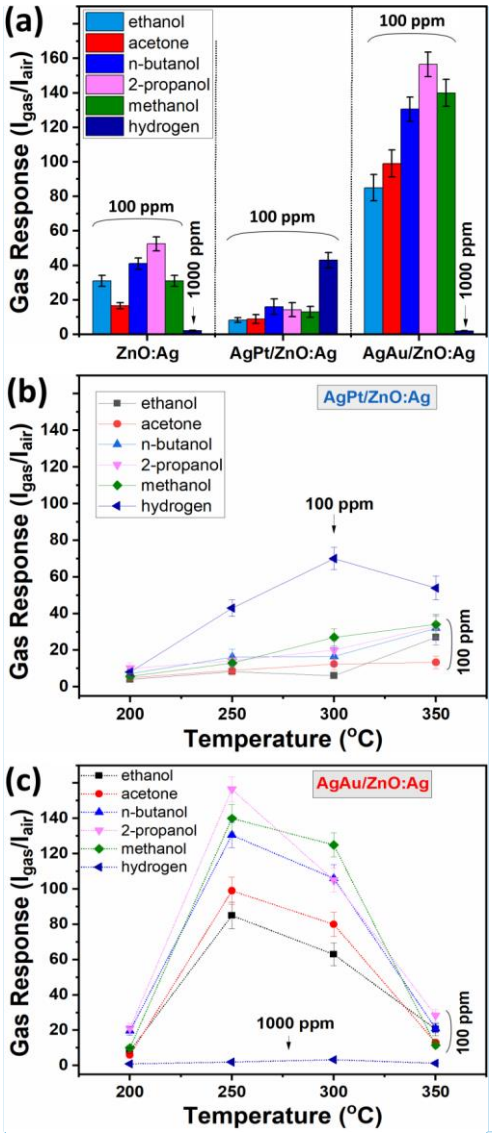

Figure 5. (a) Gas response to H_2 gas and different VOC vapors for ZnO:Ag, AgPt/ZnO:Ag and AgAu/ZnO:Ag columnar films at 250 °C operating temperature. The concentration of VOC vapors is 100 ppm. The concentration of H_2 gas is 100 ppm for the highly responsive AgPt/ZnO:Ag composite while it is 1000 ppm for the pristine ZnO:Ag thin film and AgAu/ZnO:Ag composite. Temperature dependence of the gas response for the AgPt/ZnO:Ag (b) and AgAu/ZnO:Ag (c) nanocomposite.

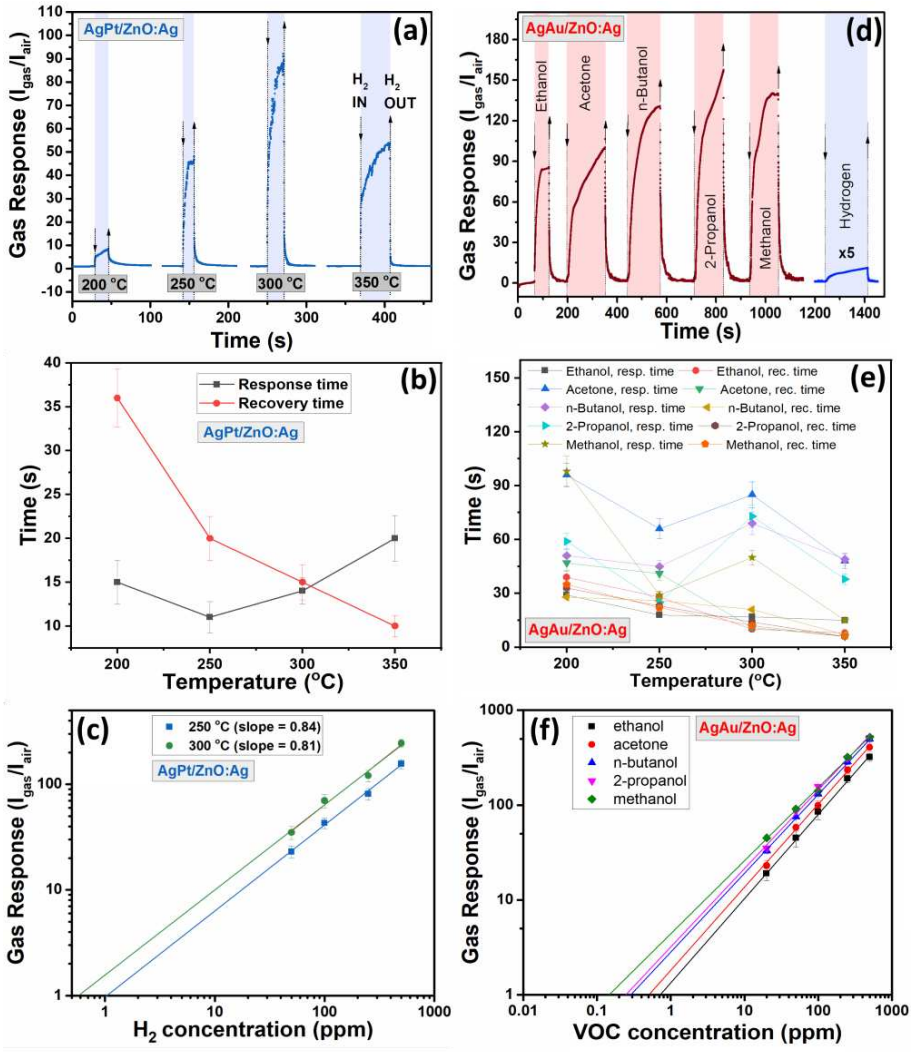

Figure 6. (a) Dynamic response of a AgPt/ZnO:Ag nanocomposite sensor to 100 ppm of H_2 gas at different operating temperatures (200 – 350 °C). (b) The response and recovery times of a AgPt/ZnO:Ag nanocomposite sensor to 100 ppm of H_2 gas versus operating temperature. (c) The dependence of H_2 gas response to H_2 gas concentration for AgPt/ZnO:Ag at 250 and 300 °C. (d) Dynamic response of a AgAu/ZnO:Ag nanocomposite sensor to 100 ppm of VOC vapors and 1000 ppm of H_2 gas at 250 °C. (e) Response and recovery times of a AgAu/ZnO:Ag nanocomposite sensor versus operating temperature for different VOCs. (f) Dependence of gas response to the concentration of VOC vapours for AgAu/ZnO:Ag at 250 °C of operating temperature.

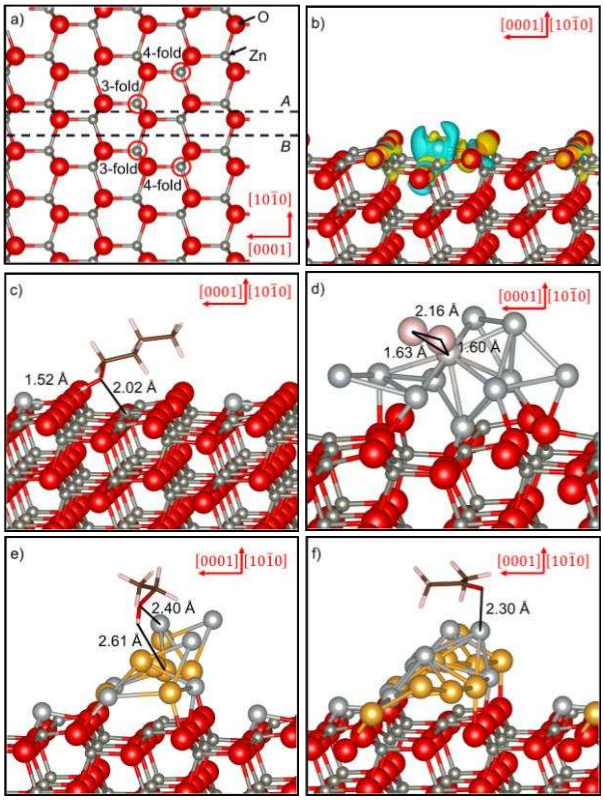

Figure 7. (a) Side view of the simulation slabs for terminations A and B of the ZnO$(10\bar{1}0)$ surface. The 3- and 4-fold Zn positions that were doped with Ag are displayed within red circles, and the dashed lines represent the surface terminations. (b) Charge density flow (ρ) for the substitutional doping using Ag of the termination B of the ZnO$(10\bar{1}0)$ surface. Electron density gain and depletion surfaces are in yellow and green, respectively. Isosurfaces display a value of ±0.002 e Å^{-3}. (c) Molecular adsorption of *n*-C_4H_9OH on the termination B of the ZnO $(10\bar{1}0)$:Ag surface. (d) Dissociative adsorption of H_2 on the termination B of the Ag_9Pt/ZnO $(10\bar{1}0)$:Ag surface. (e) Molecular adsorption of C_2H_5OH and (f) CH_3COCH_3 on the termination B of the Ag_uAu_5/ZnO $(10\bar{1}0)$:Ag surface. Crystallographic directions are indicated for all panels.

Table 1. Overview over of the calculated response and recovery times to VOC vapors at different operating temperatures.

			Temperature, °C			
			200	250	300	350
ZnO:Ag	*Ethanol*	Resp. time (s)	62	49	22	18
		Rec. time (s)	16	9	3	2
	Acetone	Resp. time (s)	114	65	41	18
		Rec. time (s)	47	11	3	2
	n-Butanol	Resp. time (s)	88	105	43	38
		Rec. time (s)	22	10	4	3
	2-Propanol	Resp. time (s)	57	65	38	24
		Rec. time (s)	16	6	4	3
	Methanol	Resp. time (s)	80	51	17	40
		Rec. time (s)	28	10	4	3
AgPt/ZnO:Ag	*Hydrogen*	Resp. time (s)	15	11	14	20
		Rec. time (s)	36	20	15	10
	Acetone	Resp. time (s)	78	21	29	20
		Rec. time (s)	36	11	5	3
	n-Butanol	Resp. time (s)	61	6	28	8
		Rec. time (s)	29	7	5	3
	2-Propanol	Resp. time (s)	113	94	43	40
		Rec. time (s)	43	15	3	2
	Methanol	Resp. time (s)	46	23	45	34
		Rec. time (s)	32	8	4	2
AgAu/ZnO:Ag	*Ethanol*	Resp. time (s)	29	18	17	15
		Rec. time (s)	39	28	10	8
	Acetone	Resp. time (s)	96	66	85	48
		Rec. time (s)	47	41	11	6
	n-Butanol	Resp. time (s)	51	45	69	49
		Rec. time (s)	28	26	21	7
	2-Propanol	Resp. time (s)	59	25	73	38
		Rec. time (s)	33	23	14	6
	Methanol	Resp. time (s)	98	29	50	15
		Rec. time (s)	35	22	12	6

Table 2. Comparison of the sensing properties for VOC and H_2 sensors based on metal oxides modified/decorated with different noble metals.

Sensing material	VOCs conc. (ppm)	Gas response (I_{gas}/I_{air}) or (R_{air}/R_{gas})	Operating temperature (°C)	Response time (s)	Recovery time (s)
Ag-ZnO films [77]	EtOH 2000	~ 2	225	5	-
Ag/ZnO nanorods [78]	EtOH 100	36.52	360	50	28
ZnO-Ag hybrids [79]	EtOH 100	101.8	370	~ 15	~ 20
Ag-ZnO nanorods [80]	EtOH 50	34.8			
	Acetone 50	25	280	-	-
	Methanol 50	14.5			
Ag-loaded ZnO [81]	EtOH 100	~ 75			
	Acetone 100	~ 30			
	Isopropanol 100	~ 68	240	-	-
	Methanol 100	~ 55			
Au-doped ZnO NWs [82]	EtOH 1000	~ 37	240	-	-
Au/ZnO NWs [6]	EtOH 100	33.6	380	3	1
Au/ZnO nanorods [83]	EtOH 100	89.5	300	2	2
Au NPs/ZnO [84]	EtOH 1000	32	300	-	-
Au/ZnO nanoplates [70]	EtOH 100	21		2	2
	Acetone 100	32	400	4	4
Au/ZnO nanoplates [85]	EtOH 100	20		13	-
	Acetone 100	16	300	-	-
	Methanol 100	7		-	-
Au/ZnO yolk-shell nanospheres [63]	Acetone 100	37	300	2	38
	Methanol 100	~ 22		-	-
Au/ZnO [64]	EtOH 50	8.9	300	10	-
	Methanol 50	~ 7			
Au@ZnO core-shell nanoparticles [7]	EtOH 100	~ 63	300	75	600
Au/T-TiZnO [86]	EtOH 50	~ 22	320	-	-
Au/flower-like ZnO [62]	EtOH 100	45.56		-	-
	Acetone 100	74.41	270	5	3
Pt/ZnO NWs [87]	EtOH 50	32.6	265	-	-
PtAu/ZnO nanorods [13]	H_2 250	~ 160	130	-	-
PtPd/ZnO nanorods [14]	H_2 10 000	~ 3	100	5	76
AgPt/ZnO:Ag columnar films (this work)	**H_2 100**	**43**	**250**	**11**	**20**
		70	**300**	**14**	**15**
	EtOH 100	8.3	250	7	12
	Acetone 100	8.9	250	21	11
	2-propanol 100	14.3	250	6	7
	n-butanol 100	16.2	250	94	15
	Methanol 100	13	250	23	8
AgAu/ZnO:Ag columnar films (this work)	EtOH 100	85		18	28
	Acetone 100	99		66	41
	2-propanol 100	**156.5**	**250**	**45**	**26**
	n-butanol 100	130.5		25	23
	Methanol 100	140		29	22

Commented [AV6]: @ Oleg: Please add here the response value for 1000 ppm H2

Table 3. Calculated surface energies after relaxation (γ_r) for terminations *A* and *B* of the pristine ZnO$(10\bar{1}0)$ surface.[42] The surface free energies (σ) are also reported for both terminations of the Ag-doped ZnO$(10\bar{1}0)$ surface. The work function (Φ) values are indicated for the pristine[42] and doped surfaces.

Termination	Doping site	γ_r/σ (meV Å^{-2})	Φ (eV)
A	pristine	190	5.40
	3-fold	172	2.50
	4-fold	176	2.61
B	pristine	84	5.80
	3-fold	125	2.84
	4-fold	130	2.64

Table 4. Calculated surface free energy (σ) and work function (Φ) for the Ag-doped ZnO$(10\bar{1}0)$ surface decorated with the Ag_5Au_5 and Ag_9Pt clusters. The adsorption energy (E_{ads}) for the NPs on the Ag-doped ZnO$(10\bar{1}0)$ surface is reported. The relative position of the NP with respect to the Ag-dopant is also indicated. The doping was carried out in the 3-fold position of termination *B*.

Cluster	Position	σ (meV Å^{-2})	E_{ads} (eV)	Φ (eV)
Ag_5Au_5	above	181	5.54	3.01
	close	184	5.88	3.10
	far	179	5.32	3.12
Ag_9Pt	above	192	6.63	2.95
	close	209	8.30	2.95
	far	194	6.79	3.15

Table 5. Adsorption energies (E_{ads}) and charge transfers (Δq) for the CH_3CH_2OH, CH_3COCH_3, *n*-C_4H_9OH, 2-C_3H_7OH, CH_3OH and H_2 molecules on the Ag-doped ZnO$(10\bar{1}0)$ surface and following decoration with the Ag_5Au_5 and Ag_9Pt clusters. The relative position of the adsorbate with respect to the dopant is also indicated. The doping was carried out in the 3-fold position of termination *B*.

Molecule	Position	ZnO$(10\bar{1}0)$:Ag		Ag_9Pt		Ag_5Au_5	
		E_{ads} (eV)	Δq (e^-)	E_{ads} (eV)	Δq (e^-)	E_{ads} (eV)	Δq (e^-)
CH_3CH_2OH	defect	-1.527	0.09	-0.590	-0.04	-0.762	0.00
	close	-1.486	0.02				
	far	-1.602	0.03				
CH_3COCH_3	defect	-1.122	0.07	-0.663	0.02	-0.798	0.00
	close	-1.021	0.04				
	far	-1.027	0.04				
n-C_4H_9OH	defect	-1.485	0.08	-0.545	0.04	-0.551	-0.02
	close	-1.632	0.03				
	far	-1.706	0.03				
2-C_3H_7OH	defect	-1.616	0.09	-0.555	0.05	-0.798	0.00
	close	-1.530	0.03				
	far	-1.597	0.03				
CH_3OH	defect	-1.469	0.08	-0.453	-0.07	-0.528	-0.02
	close	-1.425	0.02				
	far	-1.456	0.02				
H_2	defect	-1.046	0.44	-1.387	-0.07	-0.070	-0.02
	close	-0.268	0.02				
	far	-0.291	0.03				